

## Tropical Pacific Decadal Variability and ENSO Precursor in CMIP5 Models

YINGYING ZHAO,<sup>a</sup> EMANUELE DI LORENZO,<sup>a</sup> DAOXUN SUN,<sup>a</sup> AND SAMANTHA STEVENSON<sup>b</sup>

<sup>a</sup> Program in Ocean Science and Engineering, Georgia Institute of Technology, Atlanta, Georgia

<sup>b</sup> Bren School of Environmental Science and Management, University of California Santa Barbara

(Manuscript received 10 March 2020, in final form 20 October 2020)

**ABSTRACT:** Observational analyses suggest that a significant fraction of the tropical Pacific decadal variability (TPDV) (~60%–70%) is energized by the combined action of extratropical precursors of El Niño–Southern Oscillation (ENSO) originating from the North and South Pacific. Specifically, the growth and decay of the basin-scale TPDV pattern (time scale = ~1.5–2 years) is linked to the following sequence: ENSO precursors (extratropics, growth phase) → ENSO (tropics, peak phase) → ENSO successors (extratropics, decay phase) resulting from ENSO teleconnections. This sequence of teleconnections is an important physical basis for Pacific climate predictability. Here we examine the TPDV and its connection to extratropical dynamics in 20 models from phase 5 of the Coupled Model Intercomparison Project (CMIP). We find that most models (~80%) can simulate the observed spatial pattern ( $R > 0.6$ ) and frequency characteristics of the TPDV. In 12 models, more than 65% of the basinwide Pacific decadal variability (PDV) originates from TPDV, which is comparable with observations (~70%). However, despite reproducing the basic spatial and temporal statistics, models underestimate the influence of the North and South Pacific ENSO precursors to the TPDV, and most of the models' TPDV originates in the tropics. Only 35%–40% of the models reproduce the observed extratropical ENSO precursor patterns ( $R > 0.5$ ). Models with a better representation of the ENSO precursors show 1) better basin-scale signatures of TPDV and 2) stronger ENSO teleconnections from/to the tropics that are consistent with observations. These results suggest that better representation of ENSO precursor dynamics in CMIP may lead to improved Pacific decadal variability dynamics and predictability.

**KEYWORDS:** ENSO; Model comparison; Decadal variability; Tropical variability

### 1. Introduction

Pacific decadal variability (PDV), here defined as variability on time scales longer than 6–8 years, has long been recognized for its strong impacts on global climate as well as regional weather and marine ecosystems, particularly over North America and Asia (Roemmich and McGowan 1995; Mantua et al. 1997; Martinez et al. 2009; Alexander et al. 2010; Deser et al. 2010; Liu 2012; Di Lorenzo et al. 2013; Chen and Wallace 2015; Liu and Di Lorenzo 2018). Recent studies indicate that PDV had a significant contribution to the observed warming hiatus during the last decade (Meehl et al. 2013; Kosaka and Xie 2013; Watanabe et al. 2014; England et al. 2014). PDV has been described in terms of several climate modes, like the interdecadal Pacific oscillation (IPO; Trenberth and Hurrell 1994; Power et al. 1999), the Pacific decadal oscillation (PDO; Mantua et al. 1997), the North Pacific Gyre Oscillation (NPGO; Di Lorenzo et al. 2008), and the South Pacific decadal oscillation (SPDO; Garreaud and Battisti 1999; Mo 2000; Hsu and Chen 2011). These climate modes tend to share a similar pattern to El Niño–Southern Oscillation (ENSO) (Zhang et al. 1997) on decadal time scales, which indicates that tropical dynamics (e.g., ENSO) play a significant role in the PDV

(Linsley et al. 2000). Tropical Pacific decadal variability (TPDV), defined as the dominant mode of low-frequency (time scales > 8 years) sea surface temperature (SST) anomalies (SSTa) in the tropical Pacific (5°S–5°N), has an important impact on the PDV explaining about ~65% of the basin-scale variance (Zhao and Di Lorenzo 2020). TPDV and PDV are highly correlated with each other through tropical dynamics and ENSO teleconnections; however, there are important differences between the TPDV and PDV mode. The PDV mode contains important elements that are independent of the tropics, which include the decadal variability of the Kuroshio–Oyashio Extension (KOE) region in the North Pacific, the low-frequency variability of the circumpolar current in the South Pacific, and other sources (Zhao and Di Lorenzo 2020). There is a substantial body of literature that focuses on the physical mechanism of the PDV and the connection/distinction between TPDV and the other Pacific climate modes (Bratcher and Giese 2002; Liu et al. 2002; Karspeck et al. 2004; Okumura 2013; Newman et al. 2016).

The connection between PDV and TPDV is mediated through ENSO. It is well understood that ENSO teleconnections from the tropics to the extratropics project the tropical variance into the North and South Pacific regions (Alexander 1992; Alexander et al. 2002; Liu et al. 2002; Newman et al. 2003; Vimont 2005; Di Lorenzo et al. 2010; Deser et al. 2012; Liguori and Di Lorenzo 2019; Chung et al. 2019). Changes of ENSO dynamics can drive the low-frequency modulations of the Pacific mean state (Yeh and Kirtman 2005); in turn, the Pacific mean state also plays an important role in the flavors of ENSO (Choi et al. 2011).

Supplemental information related to this paper is available at the Journals Online website: <https://doi.org/10.1175/JCLI-D-20-0158.s1>.

Corresponding author: Yingying Zhao, zhaoyyw@gmail.com

DOI: 10.1175/JCLI-D-20-0158.1

© 2021 American Meteorological Society. For information regarding reuse of this content and general copyright information, consult the AMS Copyright Policy ([www.ametsoc.org/PUBSReuseLicenses](http://www.ametsoc.org/PUBSReuseLicenses)).

However, an increasing body of literature suggests that extratropical “ENSO precursors” also play an important role in energizing ENSO and TPDV (Penland and Sardeshmukh 1995; Moore and Kleeman 1996; McPhaden and Yu 1999; Fedorov 2002; Rodríguez-Fonseca et al. 2009; Kucharski et al. 2016; Liu and Di Lorenzo 2018; Liguori and Di Lorenzo 2019; Chung et al. 2019; Zhao and Di Lorenzo 2020). The extratropical ENSO precursor dynamics are initiated by perturbations in the off-equatorial trade winds during boreal winter, which in turn trigger several ocean–atmosphere mechanisms that favor the development of ENSO conditions in the summer and fall. These mechanisms include the seasonal footprinting mechanism (SFM) (Vimont et al. 2001, 2003), the trade wind charging (TWC) mechanism (Anderson 2003; Anderson et al. 2013), meridional modes (Chiang and Vimont 2004), and excitation of off-equatorial Rossby waves (Knutson and Manabe 1998). Extratropical precursors in boreal winter from both the North and South Pacific independently trigger the ENSO feedbacks in the tropics with a lead time of about 6–12 months and ENSO teleconnections to the extratropics in the following winter (Ding et al. 2015, 2017; Zhao and Di Lorenzo 2020). This progression of climate events (ENSO precursors → ENSO → ENSO successors) provides a mechanism for integrating the extratropical stochastic atmospheric seasonal variability into tropical and basin-scale low-frequency variance (Di Lorenzo et al. 2015; Zhao and Di Lorenzo 2020): we refer to this as the “TPDV hypothesis.” This mechanism can also be described in terms of a simple autoregressive process of order 1 where the memory associated with the tropical–extratropical progression acts as a reddening (e.g., a low-frequency filter) of the seasonal stochastic forcing (e.g., white noise). Through this coupling between tropics and extratropics, the North and South Pacific ENSO precursor dynamics are estimated to control a large fraction of the TPDV (~65%) and its phase in the observational record (Zhao and Di Lorenzo 2020). Furthermore, there is growing evidence suggesting that this coupling between extratropics and tropics may be responsible for prolonged sea surface temperature anomalies in the North Pacific (Di Lorenzo and Mantua 2016) and their predictability (Capotondi et al. 2019).

The observation of the Pacific extends at most to the early twentieth century and contains substantial uncertainties (Deser et al. 2010). The long-term simulations from Earth system models (ESMs), such as the simulations from the Coupled Model Intercomparison Project (CMIP), thus become powerful tools to understand the PDV and TPDV. Although these models can capture the basic spatial patterns of the dominant modes of Pacific decadal variability, their power spectra and statistics of teleconnections show distinct discrepancies (e.g., Furtado et al. 2011; Kwon et al. 2012; Park et al. 2013; Yim et al. 2014; Nidheesh et al. 2017; Yi et al. 2018). The CMIP3 generation of climate models cannot accurately capture decadal SST and sea level pressure (SLP) modes in the North Pacific or ENSO teleconnections from the tropics to extratropics (Furtado et al. 2011). Recently, there has been reported improvement of model performance in CMIP5 models with regard to dynamic fields such as wind stress (Lee et al. 2013), SSH (Landerer et al. 2014), SST, and sea level (Lyu

et al. 2016), as well as several climate models like ENSO (Kim and Yu 2012), the North Pacific Oscillation (NPO) (Rogers 1981), and the Pacific–North American teleconnection (PNA) (Chen et al. 2018). In fact, an increasing number of studies on decadal predictions have been conducted using CMIP-type models (Newman 2007; Meehl et al. 2014). To better identify the mechanistic basis for decadal predictability in the Pacific, it is important to diagnose the mechanisms of PDV and TPDV in climate models and compare them with those inferred from observations (Liu and Di Lorenzo 2018). Given the observational evidence that extratropical ENSO precursors play an integral role in TPDV (Di Lorenzo et al. 2015), Zhao and Di Lorenzo (2020) also explored the ability of climate models to capture the TPDV dynamics. They found the TPDV and PREC spatial patterns of climate models show important discrepancies from observations, and the fraction of TPDV explained by the extratropical precursors is much smaller compared to the observations. In this work, we expand previous findings by diagnosing and comparing the mechanisms that energize the TPDV and PDV across CMIP5 with the specific focus on the role of tropical/extratropical teleconnections patterns on both decadal and interannual time scales. We find that models with a better simulation of extratropical ENSO precursors also show a better TPDV pattern and stronger ENSO teleconnection. This work provides a comprehensive framework to evaluate the ability of models to reproduce realistic Pacific climate dynamics and builds the basis for decadal predictability in the Pacific.

The paper is organized as follows. The data and approaches to diagnose the TPDV are explained in section 2. Section 3 shows the spatiotemporal features of PDV and TPDV in CMIP5 models. The interaction between the extratropics and tropics outlined in the TPDV hypothesis is examined for each model in section 4. We then discuss the mechanism of tropical Pacific decadal variability in section 5 and conclude with a discussion and summary in section 6.

## 2. Datasets and methods

### a. Observational data and model outputs

The observational data that we use include monthly SLP from the National Centers for Environmental Prediction (NCEP) Reanalysis (Kalnay et al. 1996) and SST from the National Oceanic and Atmospheric Administration (NOAA) Extended Reconstruction SST dataset (ERSST) version 3 (Smith and Reynolds 2004). The monthly SLP and SST are at  $2.5^\circ \times 2.5^\circ$  and  $2^\circ \times 2^\circ$  horizontal grids, respectively. We focus on the Pacific basin (i.e.,  $100^\circ\text{E}$ – $60^\circ\text{W}$ ,  $75^\circ\text{S}$ – $60^\circ\text{N}$ ) and analyze the observational data from 1950 to 2016.

The TPDV is also examined based on the historical simulation (r1i1p1) of 20 climate models from CMIP5 archives (Taylor et al. 2012) (Table 1). Our analyses are based on outputs of monthly mean SST and SLP covering from 1861 to 2004, interpolated onto the same horizontal grids ( $1^\circ \times 1^\circ$  for the ocean and  $2.5^\circ \times 2^\circ$  for the atmosphere). Here we use the entire available period of the simulations, which end in 2004, to maximize the confidence level of the decadal analysis.

TABLE 1. List of models analyzed in the present study from the CMIP5 database. According to the spatial correlation coefficients between the simulated TPDV patterns and the observed TPDV pattern, these models are classified into Class I (the top 10 models) and Class II (the others). Each model's institute, country, name, and class are given in this table.

Institute and country	Model name	Class
Canadian Centre for Climate Modeling and Analysis (CCCma), Canada	CanESM2	II
National Center for Atmospheric Research (NCAR), United States	CCSM4	I
National Science Foundation, Department of Energy, National Center for Atmospheric Research (NSF-DOE-NCAR), United States	CESM1-CAM5	I
Centre National de Recherches Météorologiques-Centre Européen de Recherche et de Formation Avancée en Calcul Scientifique (CNRM-CERFACS), France	CNRM-CM5.2	II
CSIRO in collaboration with the Queensland Climate Change Centre of Excellence (CSIRO-QCCCE), Australia	CSIRO-Mk3.6.0	I
NOAA Geophysical Fluid Dynamics Laboratory (GFDL), United States	GFDL-ESM2M	II
NASA Goddard Institute for Space Studies (GISS), United States	GISS-E2-R	II
	GISS-E2-H	II
Met Office Hadley Centre (additional HadGEM2-ES realizations contributed by Instituto Nacional de Pesquisas Espaciais), United Kingdom	HadCM3	II
	HadGEM2-AO	I
	HadGEM2-CC	I
	HadGEM2-ES	I
Institute for Numerical Mathematics (INM), Russia	INM-CM4	II
Institute Pierre-Simon Laplace (IPSL), France	IPSL-CM5A-LR	II
	IPSL-CM5A-MR	II
Atmosphere and Ocean Research Institute (AORI; The University of Tokyo), National Institute for Environmental Studies (NIES), and Japan Agency for Marine-Earth Science and Technology (JAMSTEC), Japan	MIROC5	I
Max Planck Institute for Meteorology (MPI-M), Germany	MPI-ESM-LR	I
Meteorological Research Institute (MRI), Japan	MRI-CGCM3	II
Norwegian Climate Centre (NCC), Norway	NorESM1-M	I
	NorESM1-ME	I

Throughout the analyses, anomalies are derived by removing the climatological monthly means and a long-term linear trend.

## b. Statistical methods

### 1) TPDV AND PDV INDICES

To investigate the features and relationships of various climate modes, we extract several indices and patterns from the climate variability in the Pacific region. TPDV and PDV patterns are defined as the leading empirical orthogonal functions (EOFs) of 8-yr low-pass SSTa determined over the tropical Pacific (5°S–5°N) and the entire Pacific basin (70°S–65°N),

respectively (Table 2). The positive TPDV/PDV phases are ENSO-like warm patterns. The TPDV index and PDV index are defined as the corresponding first principal component (PC) time series of the tropical Pacific and the entire basin low-frequency SSTa (Table 2).

### 2) ENSO (NDJ) INDEX

The November–January (NDJ) ENSO index is defined as the first PC of NDJ SSTa in the tropical Pacific (5°S–5°N) (Table 2), which explains 85% of the total variance in the observations and is associated with the season of maximum ENSO anomalies.

TABLE 2. Definitions of patterns and indices used in this work.

Pattern	Definition	Index	Definition
PDV	Leading EOF of 8-yr low-pass SSTa in the Pacific basin (70°S–65°N)	PDV	Corresponding leading PC
TPDV	Leading EOF of 8-yr low-pass SSTa in the tropical Pacific (5°S–5°N)	TPDV	Corresponding leading PC
ENSO	Correlation map between ENSO index and NDJ SSTa	ENSO	Leading PC of NDJ SSTa in the tropical Pacific (5°S–5°N)
ENSO precursors	Lead correlation map between ENSO index and the preceding JFM SLPa and/or SSTa	NSLP <sub>pre</sub> , NSST <sub>pre</sub>	Project the SLPa/SSTa precursor patterns onto the JFM anomalies in the North Pacific
		SSLP <sub>pre</sub> , SSST <sub>pre</sub>	Project the SLPa/SSTa precursor patterns onto the JFM anomalies in the South Pacific
		ENSO <sub>reSLP</sub> ENSO <sub>reSST</sub>	ENSO <sub>reSLP</sub> = $a \times \text{NSLP}_{\text{pre}} + b \times \text{SSLP}_{\text{pre}}$ ENSO <sub>reSST</sub> = $a \times \text{NSST}_{\text{pre}} + b \times \text{SSST}_{\text{pre}}$
ENSO successors	Lag correlation map between ENSO index and the following JFM SLPa and/or SSTa	NSLP <sub>tele</sub> , NSST <sub>tele</sub>	Project the SLPa/SSTa successor patterns onto the JFM anomalies in the North Pacific
		SSLP <sub>tele</sub> , SSST <sub>tele</sub>	Project the SLPa/SSTa successor patterns onto the JFM anomalies in the South Pacific
PREC	Correlation map between PREC index and 8-yr low pass SSTa	PREC	$d\text{PREC}(t)/dt = \text{ENSO}_{\text{reSST}}(t) - \text{PREC}(t)/\tau$

### 3) EXTRATROPICAL ENSO PRECURSORS AND SUCCESSORS

We separate the extratropical variabilities into ENSO precursors (e.g., meridional modes) and successors (e.g., ENSO-induced teleconnections) following the same approach as in Zhao and Di Lorenzo (2020) (see Table 2). Specifically, the precursor (teleconnection) patterns are identified using lead (lag) correlation map between the NDJ ENSO index and the preceding (following) January–March (JFM) sea level pressure anomaly (SLPa) and/or SSTa. By projecting the SLPa and SSTa precursor patterns onto the JFM anomalies, we obtain the northern (N) and southern (S) precursor indices: NSLP<sub>pre</sub>, NSST<sub>pre</sub>, SSLP<sub>pre</sub>, and SSST<sub>pre</sub>. The geographic regions used to compute the projections in the North and South Pacific are 15°–62°N, 180°–130°W for NSLP<sub>pre</sub>; 72°–25°S, 170°E–80°W for SSLP<sub>pre</sub>; 10°–55°N, 160°E–100°W for NSST<sub>pre</sub>; and 60°–15°S, 180°–75°W for SSST<sub>pre</sub>. Similarly, the teleconnection indices (NSLP<sub>tele</sub>, NSST<sub>tele</sub>, SSLP<sub>tele</sub>, and SSST<sub>tele</sub>) can be calculated by projecting the teleconnection patterns onto the JFM anomalies. The domains for calculating the projections are 15°–64°N, 120°E–100°W for NSLP<sub>tele</sub>; 75°–15°S, 135°E–70°W for SSLP<sub>tele</sub>; 10°–60°N, 120°E–100°W for NSST<sub>tele</sub>; and 60°–15°S, 180°–75°W for SSST<sub>tele</sub>. A linear combination of the precursor indices in both hemispheres is used to reconstruct ENSO (Table 2): ENSO<sub>reSLP</sub> =  $a \times \text{NSLP}_{\text{pre}} + b \times \text{SSLP}_{\text{pre}}$  or ENSO<sub>reSST</sub> =  $a \times \text{NSST}_{\text{pre}} + b \times \text{SSST}_{\text{pre}}$ , where  $a + b = 1$ . The index is reconstructed with the parameter  $a$  varying from 0 to 1 with 0.1 intervals and the  $a$  and  $b$  that maximize the correlation between ENSO<sub>re</sub> and ENSO are selected. To be clear, the patterns and indices used in this work are summarized in Table 2.

To extract a measure of the ENSO precursors' contribution to tropical low-frequency variability we use the same approach

and parameters as in Zhao and Di Lorenzo (2020). We applied an autoregressive model of order 1 (AR-1) forced with ENSO<sub>reSST</sub> to obtain the low-frequency PREC index associated with the reddening of the ENSO precursor dynamics:

$$\frac{d\text{PREC}(t)}{dt} = \text{ENSO}_{\text{reSST}}(t) - \frac{\text{PREC}(t)}{\tau}.$$

In this equation, the time step  $t$  is 1 year and parameter  $\tau$  represents the memory of the coupled system, which is the decay time scale associated with the process ENSO precursors (JFM) → ENSO (OND) → ENSO successors (JFM + 1). Here  $\tau = 1.2$  years (Zhao and Di Lorenzo 2020). The correlation between PREC and TPDV indices is not very sensitive to  $\tau$  in the climate models (see Fig. S1 in the online supplemental material). When  $\tau = 1.2$  years, the correlation coefficient is close to the median in each model. This approach works well in the observations because the North and South Pacific ENSO precursors are independent of ENSO and the tropics, therefore allowing us to quantify the TPDV that originates in the extratropics. However, in the CMIP5 archive we find that not all models exhibit precursors that are independent (see discussion in section 5), especially when the models tend to exhibit a more periodic behavior in ENSO. For those models, we cannot isolate with confidence the low-frequency variance that is truly originating in the extratropics (e.g., the periodic behavior makes it difficult to isolate cause and effect). Nevertheless, we perform this standard approach to all models and discuss the results and limitations in sections 4 and 5.

### 4) SIGNIFICANCE TESTING

For all the calculations of correlation coefficients or regression coefficients in this paper, the significance is assessed

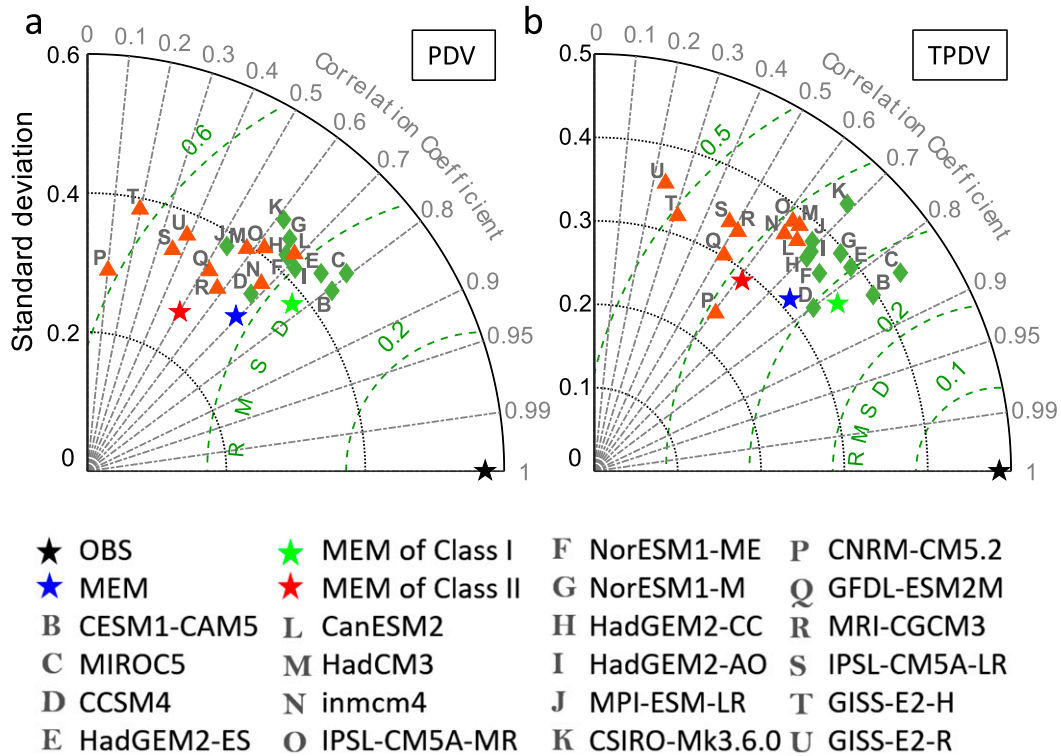


FIG. 1. Taylor diagrams for (a) PDV patterns and (b) TPDV patterns simulated in CMIP5 models. PDV/TPDV patterns are computed using correlations of the 8-yr low-pass SSTa with the PDV/TPDV indices. The black stars on the  $x$  axis signify the observational patterns based on NOAA ERSST v3 (Smith and Reynolds 2004). Green dashed circles centered at the reference points represent the root-mean-square deviation (RMSD), and gray circles centered at the origins show the normalized standard deviation (STD). Spatial correlations are shown as cosine of the angles from the  $x$  axis. MEMs and Class I (II) models are shown as stars and green diamonds (red triangles), respectively, in the figures.

by a two-sided Student's  $t$  test ( $F$  test) using the effective temporal degrees of freedom by considering serial autocorrelation (Bretherton et al. 1999). When calculating the multi-model ensemble mean (MEM) statistics, we use the arithmetic mean of the statistics analyzed in each individual model. For example, we calculate the ensemble mean of TPDV patterns as follows: 1) we obtain the TPDV pattern using the correlation map between the TPDV index and 8-yr low-pass SSTa field in each model; 2) we flip the sign if necessary to keep the positive correlation in the eastern Pacific so that the pattern always represents the positive TPDV phase; and 3) the individual TPDV patterns are averaged collectively as the MEM. Similarly, the MEM of the power spectrum is defined as the average of the individual normalized power spectra in each model.

### 3. Spatiotemporal features of PDV and TPDV in CMIP5 models

To assess the CMIP5 models' fidelity in simulating patterns of PDV and TPDV (100°E–60°W, 75°S–60°N), we plot Taylor diagrams (Taylor 2001) to evaluate the similarity between each modeled pattern and referenced pattern in terms of their

spatial correlation coefficient (SCC), standard deviation (STD), and root-mean-square deviation (RMSD) (Fig. 1). The reference points in Fig. 1 shown as black stars signify the observational patterns based on NOAA ERSST v3. In the Taylor diagrams, points that lie near the reference point indicate the corresponding models agree well with the observation. As shown in Fig. 1, the large scatter of points reveals that there are significant differences in representations of PDV (TPDV) spatial variability among CMIP5 models. All of the 20 CMIP5 models underestimate the variance of PDV and TPDV, although the magnitudes of the underestimation vary. For example, 14 (10) models show STDs of PDV (TPDV) higher than 70% of the corresponding STDs in the observation. The SCCs of the PDV pattern vary greatly from 0.1 (CNRM-CM5.2) to 0.81 (CESM1-CAM5), but there are 12 models (60%) showing SCCs greater than 0.6. Similarly, the majority of models (75%) show comparatively high SCCs (>0.6) of the TPDV pattern. The range of RMSDs of the PDV is from 0.34 (CESM1-CAM5) to 0.62 (GISS-E2-H), while that of the TPDV is from 0.26 (CESM1-CAM5) to 0.53 (GISS-E2-R). With the highest spatial correlations and the lowest RMSDs, CESM1-CAM5 reproduces PDV/TPDV patterns most similar to observations among the 20 models.

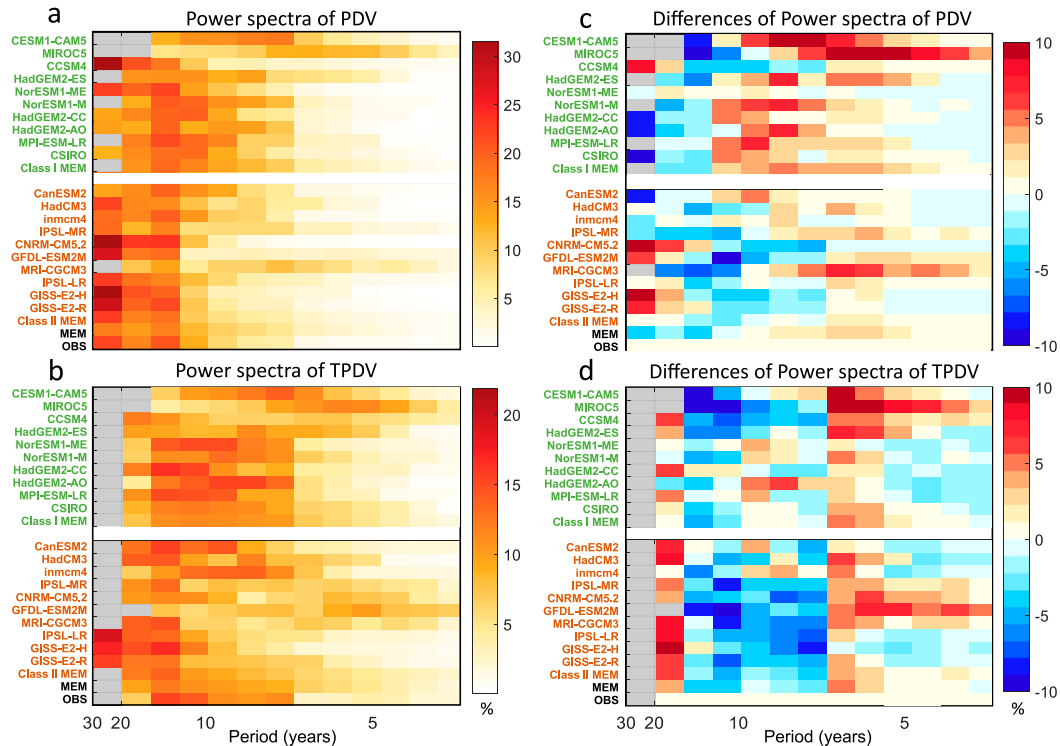


FIG. 2. Power spectra of (a) PDV and (b) TPDV indices of the observation, MEMs and the individual simulations as functions of period (years). Differences of power spectra of (c) PDV and (d) TPDV indices between the observation and the individual simulations and MEMs as functions of period (years). Different color represents the percentage of total variance explained at the specific frequency. Only significant power values (confidence level  $\geq 95\%$ ) are shaded. Models in Class I (II) are highlighted with green (red) fonts in the y axis.

To further investigate the decadal variability of the tropical Pacific, we classify these CMIP5 models into two classes in terms of the evaluations of similarity between simulated TPDV patterns with the observational patterns (Fig. 1b). The top 50% models (10 models) that show higher SCCs between simulated TPDV patterns and the observational TPDV (the mean correlation is 0.76) are selected as Class I. Specifically, they show SCCs of the TPDV pattern higher than 0.68 and RMSDs lower than 0.37. CCSM4, CESM1, MIROC5, HadGEM2-ES/AO/CC, NorESM1-M/ME, MPI-ESM-LR, and CSIRO-Mk3.6.0 belong to Class I and are shown as green diamonds in Fig. 1. Class II includes the other 10 models that lie comparatively farther from the reference point (the mean TPDV spatial correlation is 0.52), with SCCs  $< 0.68$  (shown as red triangles in Fig. 1). We find that models in Class I overall show better ability to simulate the PDV pattern compared with the models in Class II (Fig. 1a). The spatial correlations of the ensemble mean PDV (TPDV) patterns of all 20 models, 10 Class I models, and 10 Class II models are 0.69, 0.78, and 0.50 (0.75, 0.82, and 0.61) respectively, which are higher than the mean of each cluster. The MEMs also underestimate the spatial variances of PDV and TPDV: the STDs of the PDV (TPDV) pattern are about 45%–65% (60%–70%) of the reference data. From Fig. 1, the TPDV pattern is better described than the PDV pattern in CMIP5 models (smaller distances between the

models and observations in Fig. 1b vs Fig. 1a). Considering that it is more difficult for models to capture decadal variance than the interannual variance, the simulations of PDV and TPDV patterns in CMIP5 models are defective, compared with the simulation of ENSO (for more details see section 4).

To compare the temporal variability of PDV and TPDV between observations and models, we apply spectral analysis to the time series of the corresponding indices. For each individual spectrum, spectral power is normalized to represent the percentage of total variance explained at the certain frequency. Frequencies with significant power are determined if the peak exceeds the 95% confidence level with respect to a red noise null hypothesis. Note that models in Class I (II) are highlighted with green (red) fonts in Fig. 2. For the PDV, the observational power spectrum shows significant peaks on decadal time scales (10–30 years) and the ensemble mean power spectrum closely resembles the observation (Fig. 2a). More specifically, although with varying amplitudes, in most models (18 out of 20) the spectrum maximizes on the observed decadal time scales (10–30 years) (Fig. 2a). Several models (GISS-E2-R, GISS-E2-H, GFDL-ESM2M, CNRM-CM5.2, and CCSM4) show relatively more power at longer time scales ( $> 15$  years), while most of the other models show more power at shorter ( $< 10$  years) time scales (Fig. 2c). The spectral powers of the TPDV in the observation and most model simulations are not significant at

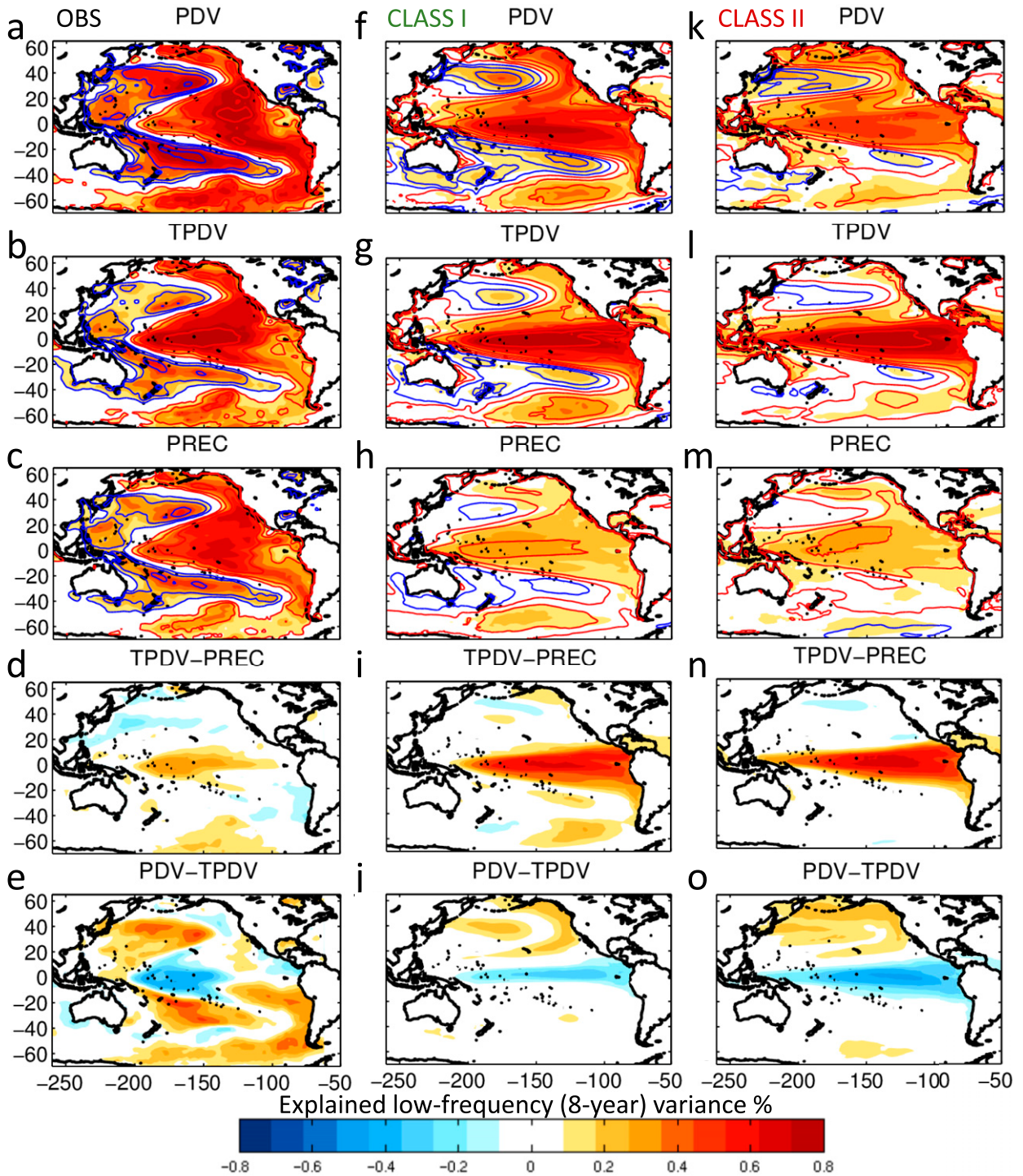


FIG. 3. (left) The shadings show the explained variances of the (a) PDV index, (b) TPDV index, and (c) PREC index to the 8-yr low pass SSTa in the OBS, and the differences of explained decadal variances between (d) the TPDV index and PREC index and (e) the PDV index and TPDV index in the OBS. The contours in (a)–(c) show the corresponding correlation maps. Contours start from  $\pm 0.3$ , and the interval is 0.2. The red contours show positive values, and the blue contours show negative values. (center) As at left, but for Class I MEM patterns. Contours start from  $\pm 0.1$ , and the interval is 0.2. (right) As at left, but for Class II MEM patterns. Contours start from  $\pm 0.1$ , and the interval is 0.2.

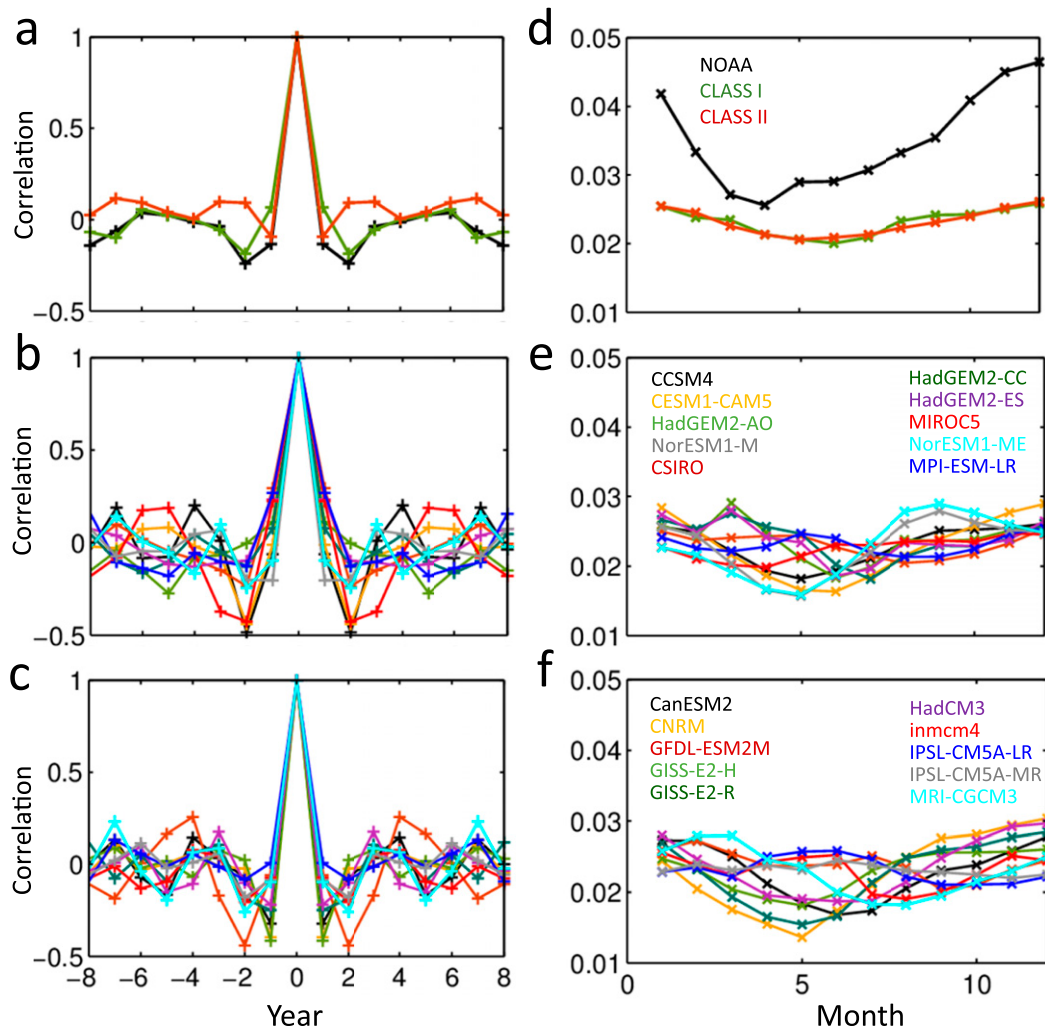


FIG. 4. (left) Autocorrelations of NDJ ENSO index of (a) observation (black line), Class I ensemble mean (green line), and Class II ensemble mean (red line); (b) Class I models; and (c) Class II models. The NDJ ENSO index is defined as the first PC of NDJ SSTa in the tropical Pacific ( $5^{\circ}\text{S}$ – $5^{\circ}\text{N}$ ). (right) Standard deviations of the monthly ENSO index defined as the first PC of monthly SSTa in the tropical Pacific ( $5^{\circ}\text{S}$ – $5^{\circ}\text{N}$ ) in different months. (d) Observational seasonality of ENSO (black line), Class I MEM ENSO seasonality (green line), and Class II MEM ENSO seasonality (red line); (e) ENSO seasonality of Class I models; and (f) ENSO seasonality of Class II models.

the 95% confidence level in the 20–30-yr period. The observation exhibits significant peaks for the TPDV index in the period range of 7–20 years and its maximum power in the 10–15-yr band with decreasing power toward higher frequencies (Fig. 2b). By contrast, the MEM has a generally lower and more uniform power spectrum in the period range of 7–20 years, as a result of averaging across models with drastically different power spectra. TPDV indices of most models (17 out of 20) show noticeable peaks at decadal time scales, especially in MRI-CGCM3, MPI-ESM-LR, and HadGEM2-ES (Fig. 2b). Compared with the observations, most models show less variance in the period range of 7–15 years and more variance at the other time scales (15–20 and <7 years) (Fig. 2d). Because of the limitation of the length of observational data (67 years), the

differences at time scales of 15–20 years are not significant. In the following analysis, the TPDV is shown to be more controlled by the extratropics in the observations, whereas in the models a larger fraction of TPDV is driven locally in the tropics (e.g., ENSO) (see Fig. 3). This may explain why models have stronger variance at time scale < 7 years. Comparing the Class I and Class II MEM spectra of TPDV and PDV, better spatial patterns do not always associate with better spectral behaviors. Overall, the temporal statistics suggest that most models can reasonably capture the decadal variability of PDV and TPDV. PDV and TPDV indices in most Class II models tend to have comparatively more power in longer time scales (20–30 years).

We now examine spatial patterns of TPDV, PDV, and PREC (e.g., the decadal variability associated with extratropical

TABLE 3. Correlation coefficients between the simulated ENSO seasonality of each model and the observed ENSO seasonality. The mean correlation coefficients of Class I and Class II models are also shown.

Class I	Correlation	Class II	Correlation
CCSM4	0.84	CanESM2	0.66
CESM1	0.89	CNRM-CM5.2	0.89
CSIRO-Mk3.6.0	0.14	GFDL-ESM2M	-0.16
HadGEM2-AO	0.28	GISS-E2-R	0.85
HadGEM2-CC	0.17	GISS-E2-H	0.90
HadGEM2-ES	0.29	HadCM3	0.92
MIROC5	0.78	INMCM4	0.22
MPI-ESM-LR	0.45	IPSL-CM5A-LR	-0.66
NorESM1-M	0.72	IPSL-CM5A-MR	-0.74
NorESM1-ME	0.65	MRI-CGCM3	0.05
Mean	0.52	Mean	0.29

ENSO precursors [see section 2b and Zhao and Di Lorenzo (2020)] in observations and Class I and II models. Figure 3 shows maps of low-frequency 8-yr low-pass SSTa variance explained by each index ( $R^2$ ) (the shading of each subplot in the first three rows shows the explained variance of TPDV, PDV, and PREC and the contour shows the corresponding correlation map). In the observation, PDV, TPDV, and PREC display similar ENSO-like patterns and explain a large fraction of the decadal variance of SSTa (40%–80%) (Figs. 3a–c). The residual explained variance of TPDV removing the influence of PREC (Fig. 3d) shows that TPDV and PREC explain similar fractions of low-frequency SSTa variance in most regions, which suggests that the low-frequency variability of the ENSO precursors is a major contributor to the basin-scale TPDV. The relatively larger differences in the tropics and Southern Ocean (Fig. 3d) indicate that the independent portion of TPDV from PREC shows more influence in these regions. Differences between the explained variance of PDV and TPDV (Fig. 3e) show that in the observation, two regions are highlighted to be independent of the tropics: the Kuroshio–Oyashio Extension (KOE) region in the North Pacific and the circumpolar current in the South Pacific (Zhao and Di Lorenzo 2020). Note that differences in the explained variance may also be linked to different representations of the zonal SST gradient across the tropical Pacific, which may impact the phase change of PDV and TPDV (Choi et al. 2013).

The PDV, TPDV, and PREC show ENSO-like patterns in the observation (Figs. 3a–c), but the Class I/II ensemble mean patterns (Figs. 3f–h,k–m) exhibit different amplitude (note that we omit  $\pm 0.1$  lines of the contour in Figs. 3a–c) and differ from their referenced counterparts (Figs. 3a–c) in certain regions, especially in the extratropics. For example, areas of negative correlations in the extratropics and the western tropics get shrunk in the ensemble means (Figs. 3f–h,k–m), especially in Class II MEM (Figs. 3k–m). The simulated PDV and TPDV can explain a large portion of the decadal variance in the tropical Pacific region (Figs. 3f,g,k,l), which generally resembles the observation (Figs. 3a,b). However, in the extratropics the simulated indices, especially TPDV of the Class II MEM (Fig. 3l), play less important roles in explaining the

low-frequency SSTa compared to observations (Figs. 3a,b). The ensemble mean PREC indices for Class I and II show quite a small influence on the decadal variance, of which Class I MEM (Fig. 3h) exhibits a comparatively similar pattern to the reference, whereas PREC of Class II MEM (Fig. 3m) lacks the dipole structure in southern extratropics and shows nearly no impact on the South Pacific. An interesting fact is that PDV, TPDV, and PREC in models of Class I have a better ability to capture the decadal variability in the extratropics, especially in South Pacific. In models, PREC explains a smaller portion of the TPDV. The residual TPDV explained variances are larger in the models (Figs. 3i,n) compared with the observation (Fig. 3d), suggesting that more fraction of TPDV is driven locally in the tropics. The MEM difference maps of the influence between PDV and TPDV (Figs. 3j,o) show that TPDV in models explains more PDV basinwide than observations and controls almost all the decadal variability in the South Pacific. In the North Pacific, the MEMs tend to show the residual revealing PDO-type variability while the KOE stands out in the observation.

In summary, Fig. 3 suggests that in models, extratropical ENSO precursor dynamics seem to play a less important role than local tropical dynamics in the decadal variability of the Pacific compared with the observations. [This can be also supported by Fig. 15a, which shows the correlation coefficients between the PDV and PREC indices (blue bars) and between the TPDV and PREC indices (green bars).] The correlations are much smaller in the models than the observation, which means the decadal extratropical precursor dynamics overall play a less dominant role in CMIP5 models. Models in Class I, which can simulate better TPDV and PDV patterns, seem to exhibit a relatively stronger connection between tropics and extratropics (e.g., the TPDV pattern has stronger projections in the higher latitudes; Fig. 3g). However, it is worth noting that the MEM is an arithmetic average of patterns but individually each model can show quite different PDV and TPDV patterns (Figs. S2 and S3). In fact, by exploring the individual patterns of TPDV and PDV in each model, we find that each model captures selected aspect of the PDV and TPDV dynamics, which in the average translate into a better PDV and TPDV representation. This is also evident from the Taylor diagram of Fig. 1 where the MEM of Class I and II is better than any individual model.

#### 4. The interaction between tropics and extratropics

In this section, we examine how ENSO precursor dynamics are simulated and to what degree the interaction between tropics and extratropics is captured in the CMIP5 climate models.

In the observations, the teleconnections between tropics and extratropics follow a clear seasonal locking with ENSO [e.g., ENSO precursors (JFM)  $\rightarrow$  ENSO (NDJ)  $\rightarrow$  ENSO teleconnections (the following JFM)]. We therefore explore the seasonality of ENSO. First, we inspect the autocorrelation function of the NDJ ENSO index to evaluate the tendency of models to have periodicity in ENSO. No strong autocorrelation is found in the MEMs, which is similar to the observation

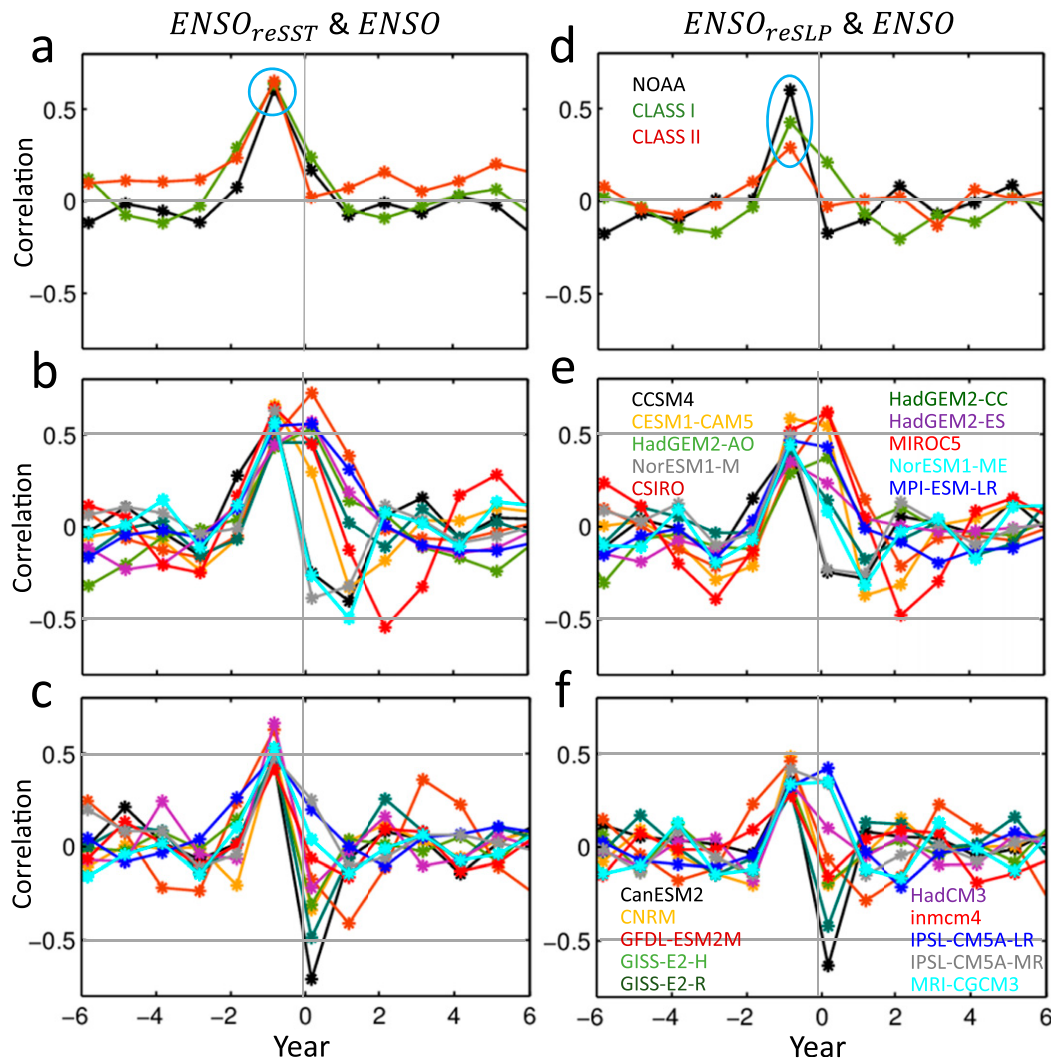


FIG. 5. Cross correlations between NDJ ENSO index and  $ENSO_{reSST}$  index of (a) observation (black line), Class I MEM (green line), and Class II MEM (red line); (b) individual models of Class I; and (c) individual models of Class II. Also shown are cross correlations between the NDJ ENSO index and  $ENSO_{reSLP}$  index of (d) observation (black line), Class I MEM (green line) and Class II MEM (red line); (e) individual models of Class I; and (f) individual models of Class II.

(Fig. 4a). However, in some individual models, ENSO shows high autocorrelation (with a correlation coefficient of about  $-0.5$ ) at a 2-yr (like CCSM4, CESM1, MIROC5, and GFDL) or 1-yr (GISS-E2-H) lead/lag (Figs. 4b,c). Thus in these models, ENSO is more periodic, which makes it more difficult to separate the independent component of ENSO precursors in the extratropics (see also section 2). Then we quantify the seasonality of ENSO through the standard deviations of the ENSO index in different months as indicated in Figs. 4d–f (Bellenger et al. 2014; Ham and Kug 2014). We find that the ENSO monthly standard deviations and the amplitudes of the seasonal variations (seasonality) of the ENSO index are overall smaller in the MEMs compared with the observation. Among the models, the amplitude of ENSO seasonality of Class I MEM (green line in Fig. 4d) is almost equal to Class II

MEM (red line in Fig. 4d). Even though the MEMs show peak of variation in winter, which is consistent with observation, some models show maximum variance in other seasons. For example, in most Class I models, ENSO reaches its maximum in winter or spring except in NorESM1-M/ME, which have stronger variability in autumn, and MPI-ESM-LR/CSIRO, which have smaller variability of ENSO seasonality. Some models, including both Class I models (CESM1/CCSM4/MIROC5) and Class II models (CNRM/HadCM3/GISS-E2-H/GISS-E2-R), show ENSO seasonal locking similar to the observations, with correlation coefficients between the simulated ENSO seasonality and the observation higher than 0.75 (Table 3). The mean correlation coefficient of Class I models (0.52) is higher than that of Class II models (0.29).

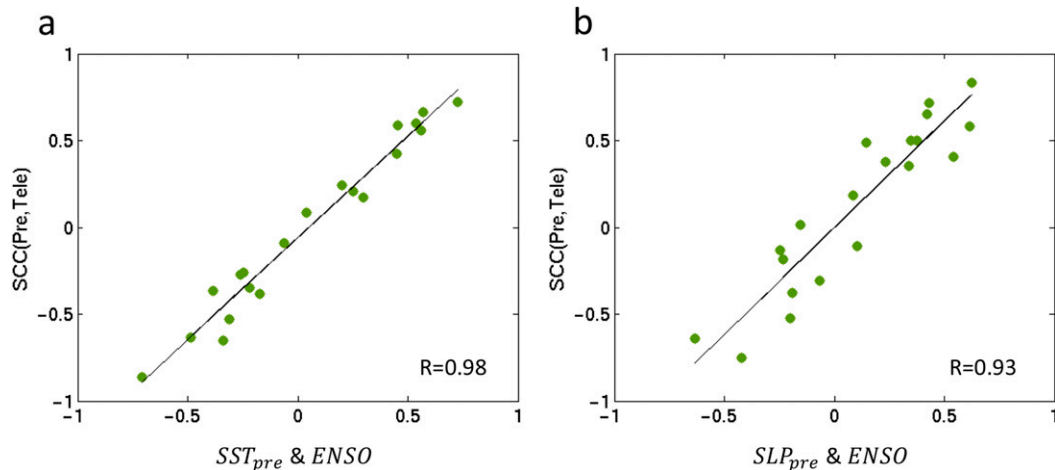


FIG. 6. (a) Scatters of the spatial correlation coefficients between extratropical SST precursor pattern and extratropical SST teleconnection pattern against the lag-0 correlation coefficients between  $SST_{pre}$  and ENSO indices. (b) Scatters of the spatial correlation coefficients between extratropical SLP precursor pattern and extratropical SLP teleconnection pattern against the lag-0 correlation coefficients between  $SLP_{pre}$  and ENSO indices. Different points represent different CMIP5 models. Also indicated are the correlation coefficients between the correlations, which pass the 99% confidence level.

To identify the ENSO variability related to precursor dynamics, we reconstruct the ENSO index with SST and SLP precursor indices using a linear model:  $ENSO_{reSST} = a \times NSST_{pre} + b \times SSST_{pre}$  and  $ENSO_{reSLP} = a \times NSLP_{pre} + b \times SSLP_{pre}$ , where  $a + b = 1$  (see section 2). In the observation, the correlation coefficient between  $ENSO_{re}$  and ENSO is maximum when  $a = 0.5$  and  $b = 0.5$ . In most models (19 out of 20 models), the values of  $a$  and  $b$  are also close. This indicates that the precursor dynamics in the South Pacific are also important to ENSO. Based on the cross-correlation analysis between the ENSO index and  $ENSO_{re}$  index, we can estimate how much ENSO variability (NDJ) is associated with ENSO precursor dynamics (JFM in the same year) (Fig. 5). In both the observation and MEMs,  $ENSO_{re}$  exhibits the highest correlation with ENSO when precursors (JFM) lead ENSO (same year NDJ) by 10 months (blue circles in Figs. 5a,d). The SLP precursor dynamics contribute about 36% to the variance of ENSO ( $R \sim 0.6$ ) when precursors lead 10 months in the observation and Class I MEM (Fig. 5d, black and green lines), whereas for Class II MEM, the maximum correlation is only 0.3 (Fig. 5d, red line). This suggests that the SLP precursor dynamics are very important in producing a better simulation of TPDV in CMIP5 models. We also find peaks in the cross-correlations at lag 0 (e.g., ENSO leads precursors by 2 months) in some models (Figs. 5b,c,e,f). To quantify how many models suffer from having precursor indices that share lag-0 correlation with ENSO, we have further examined Fig. 5. We find that five models in Class I (CSIRO, HadGEM2-AO, HadGEM2-CC, HadGEM2-ES, and MPI-ESM-LR) (Fig. 5b) and four models in Class II (CanESM2, CNRM, and GISS-E2-H/R) (Fig. 5c) exhibit lag-0 correlations between precursors and ENSO that are larger or equal to lag-1 (e.g., precursor lead ENSO 10 months). To further understand the reasons behind the lag-0 correlation between the precursor patterns and

ENSO, we examine the relation (e.g., correlation) between precursors (JFM) and ENSO teleconnection (JFM + 1) patterns in the models. The geographic region for SST spatial correlation is  $10^{\circ}$ – $55^{\circ}$ N,  $160^{\circ}$ E– $100^{\circ}$ W and  $60^{\circ}$ – $15^{\circ}$ S,  $180^{\circ}$ – $75^{\circ}$ W, and for SLP spatial correlation is  $15^{\circ}$ – $62^{\circ}$ N,  $180^{\circ}$ – $130^{\circ}$ W and  $72^{\circ}$ – $25^{\circ}$ S,  $170^{\circ}$ E– $80^{\circ}$ W, which are the same as the regions that we used to obtain the precursor indices. We find that when this correlation is high in a given model, that lag-0 correlation between the precursor (JFM) and ENSO (OND) is also very high (Fig. 6). The implication is that in these models it is either difficult to cleanly separate the precursors and teleconnection patterns in the analysis because they have a non-orthogonal spatial footprint or it may indicate that the precursor and teleconnection pattern is driven by the tropics through the development of ENSO. Despite the fact that we cannot clearly identify the existence of an extratropical precursor dynamics in these models, the key result is still important as it indicates a divergence of the model ENSO phenomenology from observations. [We also plotted the analyses of Figs. 3, 8, and 10 by excluding the nine models that have precursors with lag-0 correlation with ENSO in the supplemental information (Figs. S6–S8) and found the same ensemble mean patterns of decadal variability (Fig. S6) and interannual variability (Fig. S7). In Fig. S8, the correlation between spatial correlations of PDV and spatial correlations of South Pacific oceanic precursor changes from 0.58 to 0.36, but other correlations do not change significantly and in some cases are higher compared with Fig. 10.]

Taylor diagrams are used to assess the fidelity of CMIP5 models to simulate the spatial pattern of ENSO precursor and ENSO ( $100^{\circ}$ E– $60^{\circ}$ W,  $75^{\circ}$ S– $60^{\circ}$ N) (Fig. 7). Model ensemble means can capture the overall spatial patterns of ENSO, with the SCCs of SSTa (SLPa) patterns reaching 0.85 (0.92), but they underestimate the standard deviations of ENSO patterns

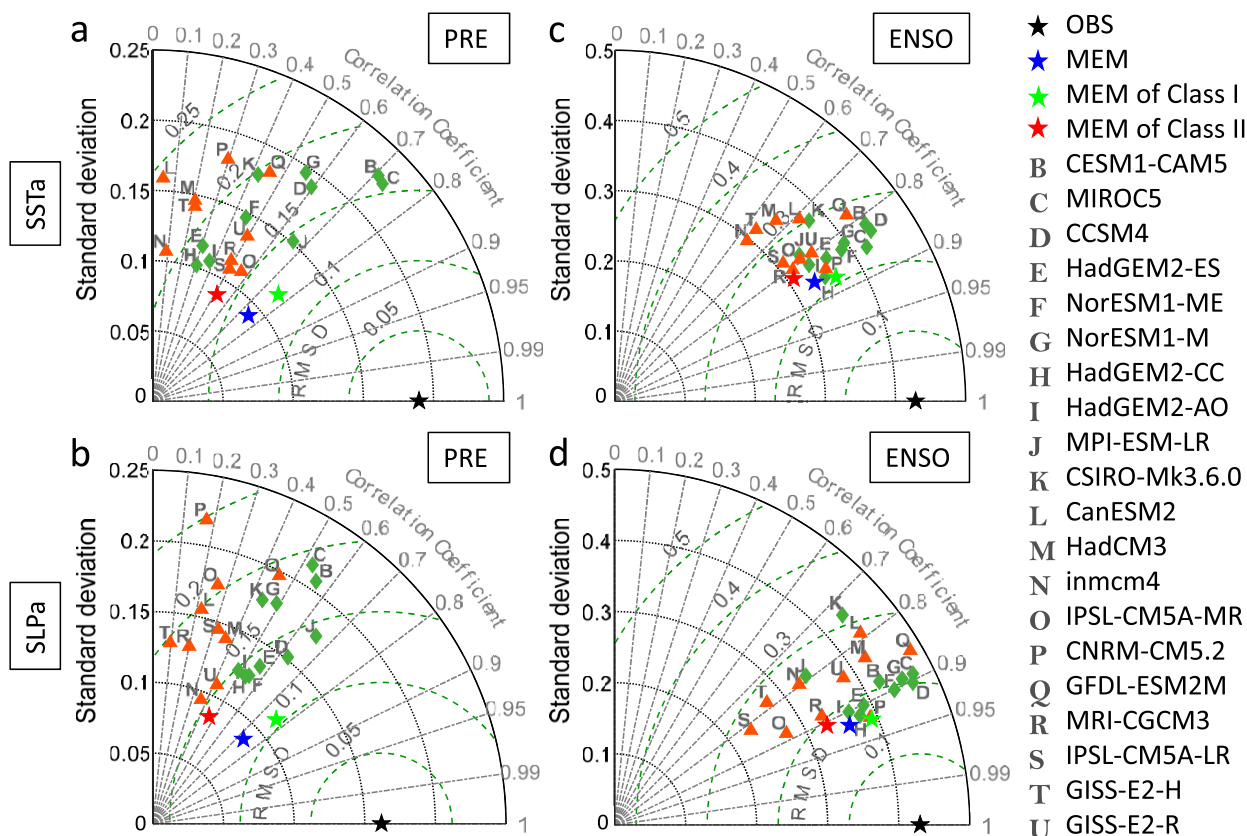


FIG. 7. Taylor diagrams for (a) ENSO SSTA precursor patterns, (b) ENSO SLPa precursor patterns, (c) ENSO SSTA patterns, and (d) ENSO SLPa patterns simulated in CMIP5 models. The black stars on the x axis signify the observational patterns. MEMs and Class I (II) models are shown as stars and green diamonds (red triangles), respectively, in the Taylor diagrams.

(stars in Figs. 7c,d). There is tendency for models that exhibit ENSO amplitudes that are stronger and close to observed values to better capture the TPDV characteristics. However, this link is not statistically significant. All of 20 CMIP5 models can reproduce the basic ENSO patterns, with SCCs  $> 0.63$  ( $0.74$ ) for SST (SLP) output (Figs. 7c,d). In 14 out of 20 models, STDs of the ENSO SLPa pattern stay within  $1\% \pm 20\%$  of the observational value (Fig. 7d). For the SST field, CESM1-CAM5, CCSM4, MIROC5, and GFDL-ESM2M show nearly the same STDs with the reference, with the others underestimating the observed spatial variability (Fig. 7c). The RMSD values range from 0.22 to 0.33 in SST and from 0.17 to 0.31 in SLP. ENSO patterns of most models in Class I (green diamonds) show better agreement with the observation, with SCCs larger than 0.8 (except MPI-ESM-LR and HadGEM2-AO).

Unlike the similarities between observed and modeled ENSO patterns, the simulations of the North and South Pacific ENSO precursor patterns in CMIP5 models are more scattered, with SCCs ranging from 0.05 (CanESM2) to 0.73 (MIROC5) in the SST field and from 0.10 (GISS-E2-H) to 0.66 (MPI-ESM-LR) in SLP field (Figs. 7a,b). Only seven models can capture the basic ENSO precursor patterns (including both the south and north expressions) with spatial correlation

coefficients higher than 0.5 in both SLP and SST fields. As for the spatial variance, 9 (8) out of 20 models show STDs of the SSTA (SLPa) pattern within the range of  $1\% \pm 20\%$  compared with the observational data. Although the bias of the ENSO precursor simulation among CMIP5 models is large, the ensemble means of all the 20 models and 10 Class I models exhibit the overall spatial patterns (Fig. 8d), with SCCs around 0.75 for both SSTA and SLPa patterns (Figs. 7a,b). The Class II MEM displays comparatively lower SCCs (0.51/0.46) but is still higher than the individual models. The differences between precursor patterns of Class I MEM and Class II MEM are mainly distributed in the southern extratropics (Figs. 8d,g). Note that all the ensemble means underestimate the spatial variance of ENSO precursor patterns, especially the MEM of Class II. Most models in Class I can reproduce a relatively better SLPa precursor pattern (Fig. 8d, blue contours); however, for the simulation of SSTA patterns, some models in Class I perform well (e.g., MIROC5 and CESM1-CAM5) while some do not (e.g., HadGEM2-ES/CC). This finding is likely related to the fact that the atmospheric precursor is always associated with the weakening of the off-equatorial winds that can initiate different types of oceanic precursor dynamics (e.g., SFM, TWC, and Rossby waves) in different models, which may be caused by differences in air-sea coupling strength and convective

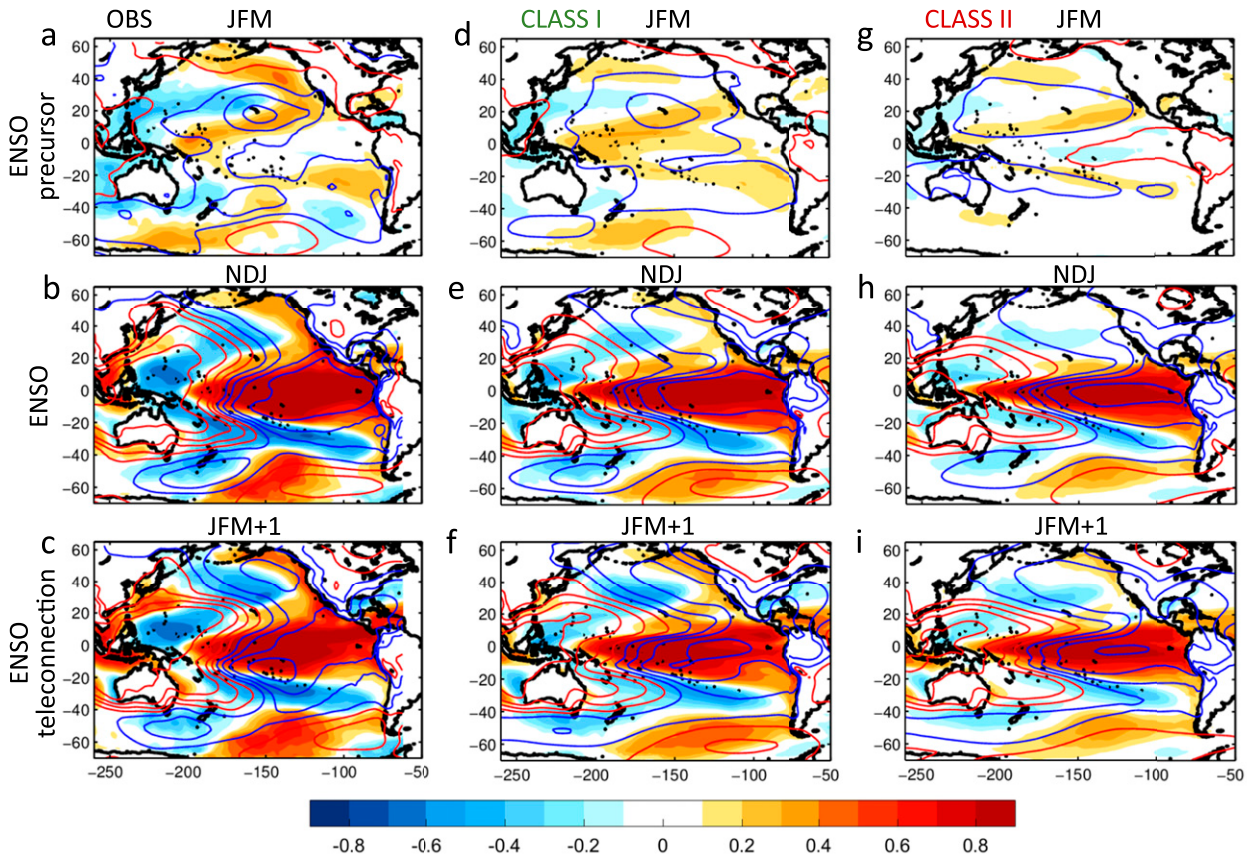


FIG. 8. ENSO precursor, ENSO, and ENSO teleconnection patterns. (left) The shadings show correlation maps between the observed NDJ ENSO index and NOAA SSTa in (a) JFM, (b) NDJ, and (c) the following JFM; the contours show correlation maps between the observed NDJ ENSO index and NCEP SLPa in (a) JFM, (b) NDJ and (c) the following JFM. The red contours show positive values, and the blue contours show negative values. Contours start from  $\pm 0.1$ , and the interval is 0.2. (center) As at left, but for Class I MEM. (right) As at left, but for Class II MEM.

excitation across models. We also separate the SSTa precursor pattern into the North Pacific (NP) part and the South Pacific (SP) part and compare their Taylor diagrams (Fig. 9). In these CMIP5 models, the NP SSTa precursor pattern is better simulated compared with the SP pattern. Specifically, 60% of the models (12 out of 20) can capture the NP precursor pattern (SCCs > 0.6) (Fig. 9a), whereas for the SP precursor only three models show SCC larger than 0.6 and Class II models usually come with weaker southern SSTa precursor dynamics (Fig. 9b).

The comparison between the observational and MEM patterns of ENSO precursor, ENSO, and ENSO successor (Fig. 8) shows clear differences between models. The NP SSTa precursor pattern in the observation (Fig. 8a) is characterized by the typical footprinting pattern, which is well reproduced by all the ensemble means (Figs. 8d,g). The SP SSTa precursor of Class I MEM (Fig. 8d) displays a similar pattern to the quadruple structure of the observation, which Class II MEM does not capture (Fig. 8g). In the observation, the atmospheric precursor pattern (contours in Fig. 8a) shows a dipole structure in both the northern and southern

extratropics, which is well presented in Class I MEM but not in Class II MEM (Figs. 8d,g). The basic observational ENSO and ENSO successor patterns (Figs. 8b,c) reemerge in the MEMs (Figs. 8e,f,h,i), but with weaker signals in the extratropical Pacific, especially in Class II MEM. In models, both the teleconnections from tropics to extratropics and the connections from extratropics to tropics are weaker compared to observations. Models that better capture the ENSO precursors (e.g., connections from extratropics to tropics) also have better teleconnections from tropics to extratropics (Fig. 8f vs Fig. 8i). To sum up, the connection between tropics and extratropics is weaker in models compared with the observation, and Class I models are revealed to have stronger connections than Class II models.

The Taylor diagrams (Fig. 7) and spatial patterns (Fig. 8) of ENSO precursors analyzed above reveal that models in Class I, which can simulate better TPDV and PDV patterns, can also reproduce better SLPa and the South Pacific SSTa precursor patterns. As is shown in Figs. 10a and 10c, the SCCs of the SLPa precursor pattern (including both the south and north expressions) are highly correlated with the SCCs of the PDV

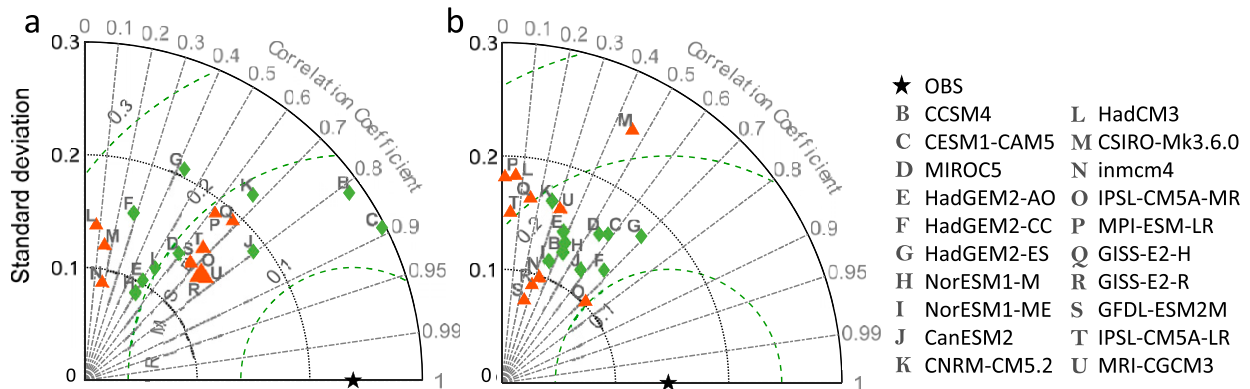


FIG. 9. Taylor diagrams for (a) North Pacific oceanic precursor patterns and (b) South Pacific oceanic precursor patterns simulated in 20 CMIP5 models. The black stars on the  $x$  axis signify the observational patterns based on NOAA ERSST v3 (Smith and Reynolds 2004). Green dashed circles centered at the reference points represent the root-mean-square deviation (RMSD), and gray circles centered at the origins show the normalized standard deviation (STD). Spatial correlations are shown as cosine of the angles from the  $x$  axis. Class I (II) models are shown as green diamonds (red triangles) in the Taylor diagrams.

( $R = 0.62$ )/TPDV ( $R = 0.62$ ) pattern in CMIP5 models. A similar relationship also exists between the SCCs of the SP SSTa precursor pattern and SCCs of the PDV ( $R = 0.58$ )/TPDV ( $R = 0.53$ ) pattern (Figs. 10b,d). Altogether these findings suggest that a good representation of SLPa precursor

patterns is important to reproduce the observed PDV and TPDV patterns in CMIP5 models. For SSTa precursor patterns, models in general show better representation the North Pacific precursors. Improvement in South Pacific skill is more important to simulate the decadal variability of the Pacific.

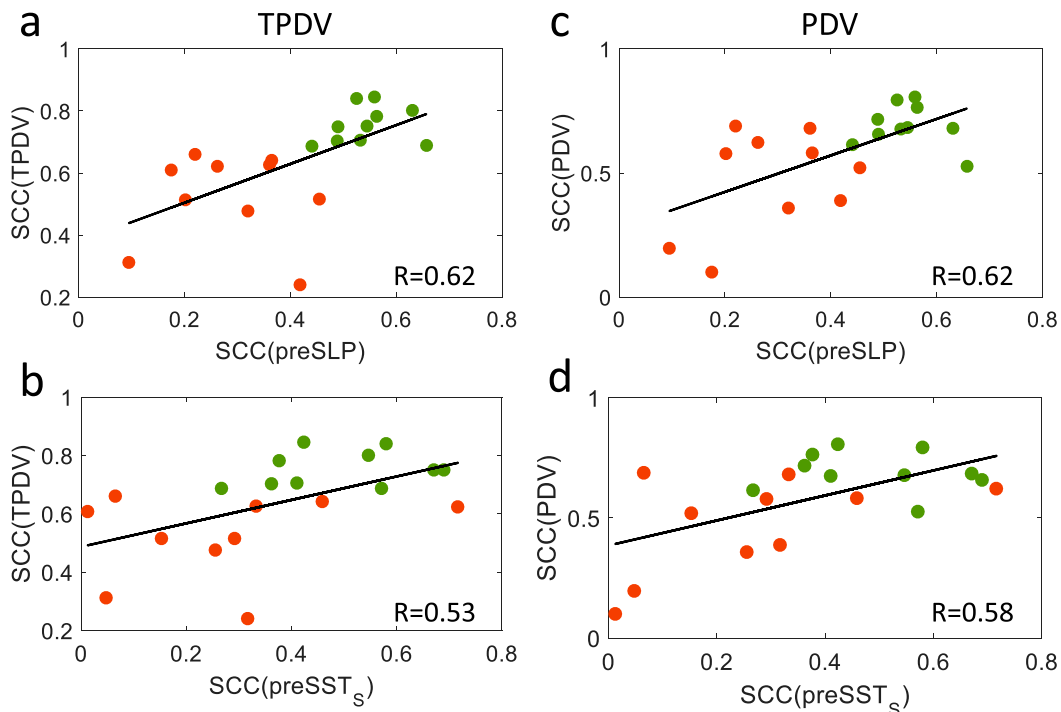


FIG. 10. (a) Scatters of the TPDV spatial correlation coefficients (SCCs) against the SCCs of ENSO atmospheric precursor patterns. (b) Scatters of TPDV SCCs against the SCCs of South Pacific oceanic precursor patterns. (c) Scatters of PDV SCCs against the SCCs of ENSO atmospheric precursor patterns. (d) Scatters of PDV SCCs against the SCCs of South Pacific oceanic precursor patterns. Class I (II) models are shown as green (red) points. Also indicated are the correlation coefficients between the SCCs. The correlation coefficients in (a), (c), and (d) pass the 99% confidence level. The correlation coefficient in (b) passes the 95% confidence level.

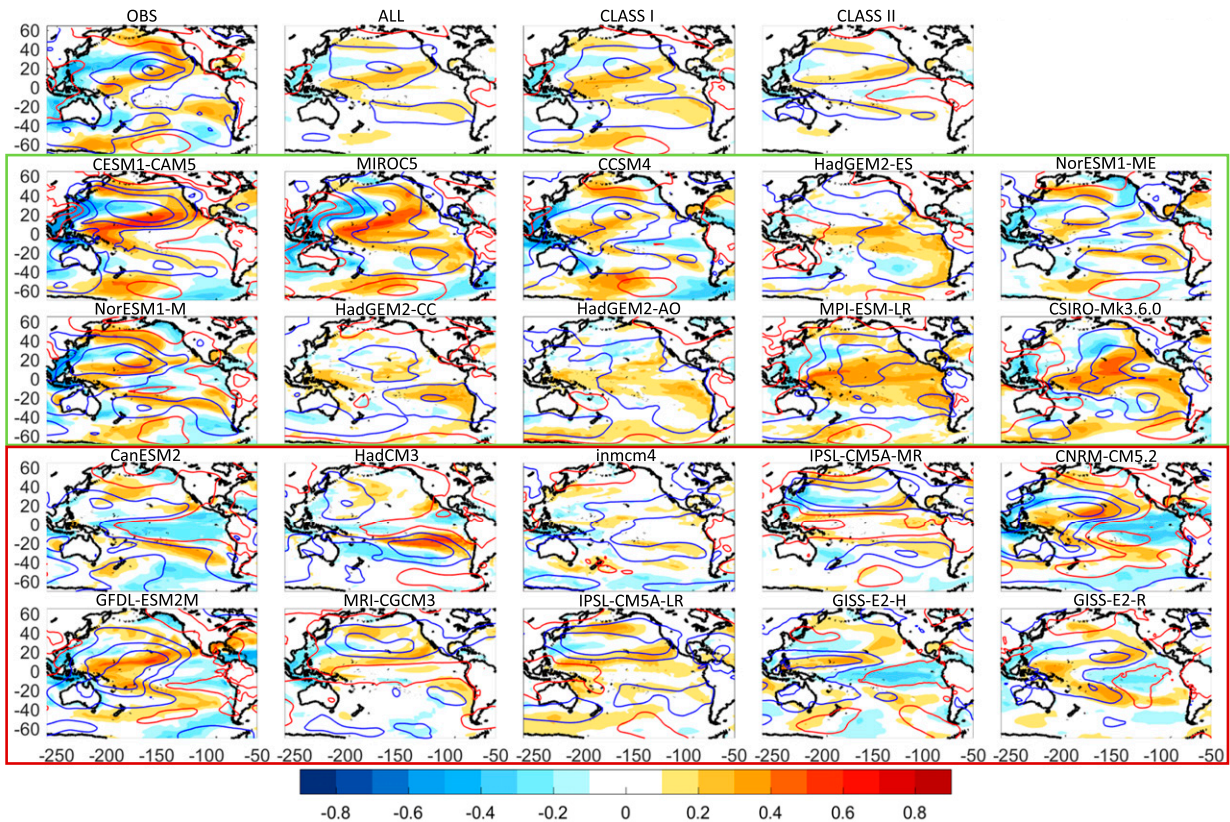


FIG. 11. ENSO precursor patterns of the OBS, ensemble means of all 20 simulations/Class I simulations/Class II simulations and individual simulations. Shadings show the oceanic precursor patterns and contours show the atmospheric precursor patterns. The red contours show positive values, and the blue contours show negative values. Contours start from  $\pm 0.1$ , and the interval is 0.2. Figures in the green (red) box exhibit precursors of Class I (II) models.

Then we inspect ENSO precursor and teleconnection patterns of each individual model in CMIP5, as shown in Figs. 11 and 12, to investigate the individual differences. Not all models of Class I can capture the overall SSTa precursor pattern (shadings in Fig. 11). For example, the simulated locations of the horseshoe-shaped structure in the North Pacific oceanic precursor of NorESM1-M/ME models are more westward compared with the referenced counterparts. However, almost all Class I models exhibit relatively better representations of the SLPa precursor and the southern SSTa precursor dynamics, which further prove that they are important for simulations of PDV and TPDV in CMIP5 models. Furthermore, most models in Class II show reasonable northern oceanic precursor patterns (SCCs > 0.6; Fig. 9a), but they do not have the same level of skill to reproduce the atmospheric precursor (Fig. 7b) and the southern oceanic precursor patterns (Fig. 9b). Note that SSTa precursor patterns of many Class I models (HadGEM2-AO/CC/ES, MIROC5, CSIRO-Mk3.6.0, and MPI-ESM-LR) exhibit relatively more signal in the tropics and resembles the ENSO pattern (Fig. 11), which indicates that in these models, the dynamics of the tropics play an important role in energizing ENSO. These discrepancies in the spatial structure of precursor dynamics across the basin lead to an ensemble model mean that is similar to the observation but

with an overall weaker decadal variance. This reflects the fact that models emphasize different aspects of the precursor dynamics even though the ensemble mean is similar to observations. The basinwide ENSO teleconnection pattern is generally reproduced by the selected models (Fig. 12), with some notable differences among the models. The simulations of ENSO teleconnection capture the strong positive correlation in the tropical Pacific but apparently underestimate the variability in the northern and southern extratropics (Fig. 12). Combining Figs. 11 and 12, we find that ENSO precursor and ENSO teleconnection patterns of Class I models show stronger signals in the extratropics compared with the patterns of Class II models, which implies that in CMIP5 models, the interannual connections between tropics and extratropics are crucial also for better representing the decadal variability in the Pacific.

## 5. The mechanism of tropical Pacific decadal variability

The connection and exchange dynamics between extratropics and tropics are important mechanisms of the multiyear climate memory of the ocean-atmosphere system, which leads to the ENSO-like TPDV (Di Lorenzo et al. 2015). In observations (ERSST v3), the North Pacific and South Pacific precursors influence ENSO independently and their expression is

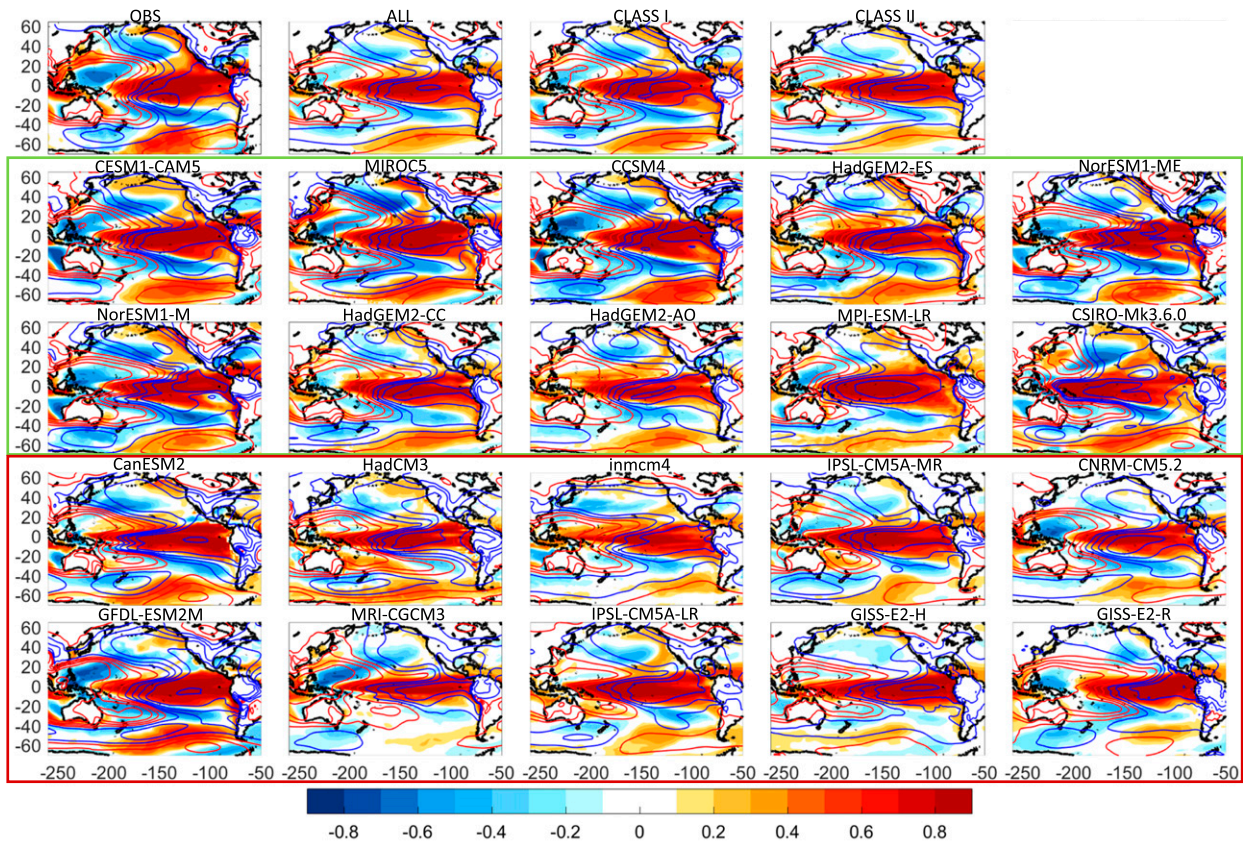


FIG. 12. ENSO teleconnection patterns of the OBS, ensemble means of all 20 simulations/Class I simulations/Class II simulations and individual simulations. Shadings show the oceanic teleconnection patterns and contours show the atmospheric teleconnection patterns. The red contours show positive values, and the blue contours show negative values. Contours start from  $\pm 0.1$ , and the interval is 0.2. Figures in the green (red) box exhibit teleconnections of Class I (II) models.

also independent of ENSO (Ding et al. 2015, 2017). ENSO plays a vital role in harmonizing the two hemispheres by exciting teleconnections into the extratropics through the atmospheric bridge. Thus after ENSO, the oceanic and atmospheric imprints of the ENSO teleconnections (e.g., successors) in the North and South Pacific are correlated with each other (Zhao and Di Lorenzo 2020).

To determine how northern and southern extratropical dynamics influence ENSO in the CMIP5 models, we compare the Class I MEM patterns of ENSO progression in different seasons developing from the North Pacific precursor (Figs. 13a–d) and the South Pacific precursor (Figs. 13e–h). Patterns of ENSO originating from the northern precursor display a southward movement of SLPa in the North Pacific (contours in Figs. 13a–c), which changes the wind stress, and then inject the SST anomalies into the tropical Pacific (shadings in Figs. 13a–c) through precursor dynamics (e.g., meridional modes). Similarly, patterns of ENSO correlated with the southern precursor show a meridional propagation of atmospheric signals from the midlatitudes to low latitudes (contours in Figs. 13e–g) and the corresponding northward movement of SST anomalies (shadings in Figs. 13e–g). More specifically, in JFM, precursor patterns in the northern and southern extratropics

are different from each other (Figs. 13a,e). Then the individual precursor energizes ENSO through different dynamics in April–June (AMJ) (Figs. 13b,f), which makes ENSO grow and peak in October–December (OND) (Figs. 13c,g). ENSO in turn projects back into the North and South Pacific in the following JFM and leads to similar ENSO teleconnection patterns (Figs. 13d,h). The progressions of ENSO developing from northern and southern precursors are similar to the observation (see Fig. S5) (Zhao and Di Lorenzo 2020). Similarly, the Class II MEM seasonal evolutions of the northern precursor (Fig. 13, third column) and southern precursor (Fig. 13, fourth column) are identified using the same correlation analysis. In Class II models, the northern precursor dynamics can transfer seasonal variance originating in the North Pacific into both hemispheres by energizing ENSO and its teleconnections (Figs. 13i–l), although with weaker variance compared to Class I. However, Class II MEM South Pacific precursor cannot develop into the typical ENSO-like interhemispheric pattern (Figs. 13m–p), implying that models that cannot represent TPDV and PDV well usually lack a southern precursor dynamics that has a Pacific-wide footprint.

We calculate the correlations between northern and southern precursor indices ( $NSLP_{pre}$  and  $SSLP_{pre}$ ,  $NSST_{pre}$  and

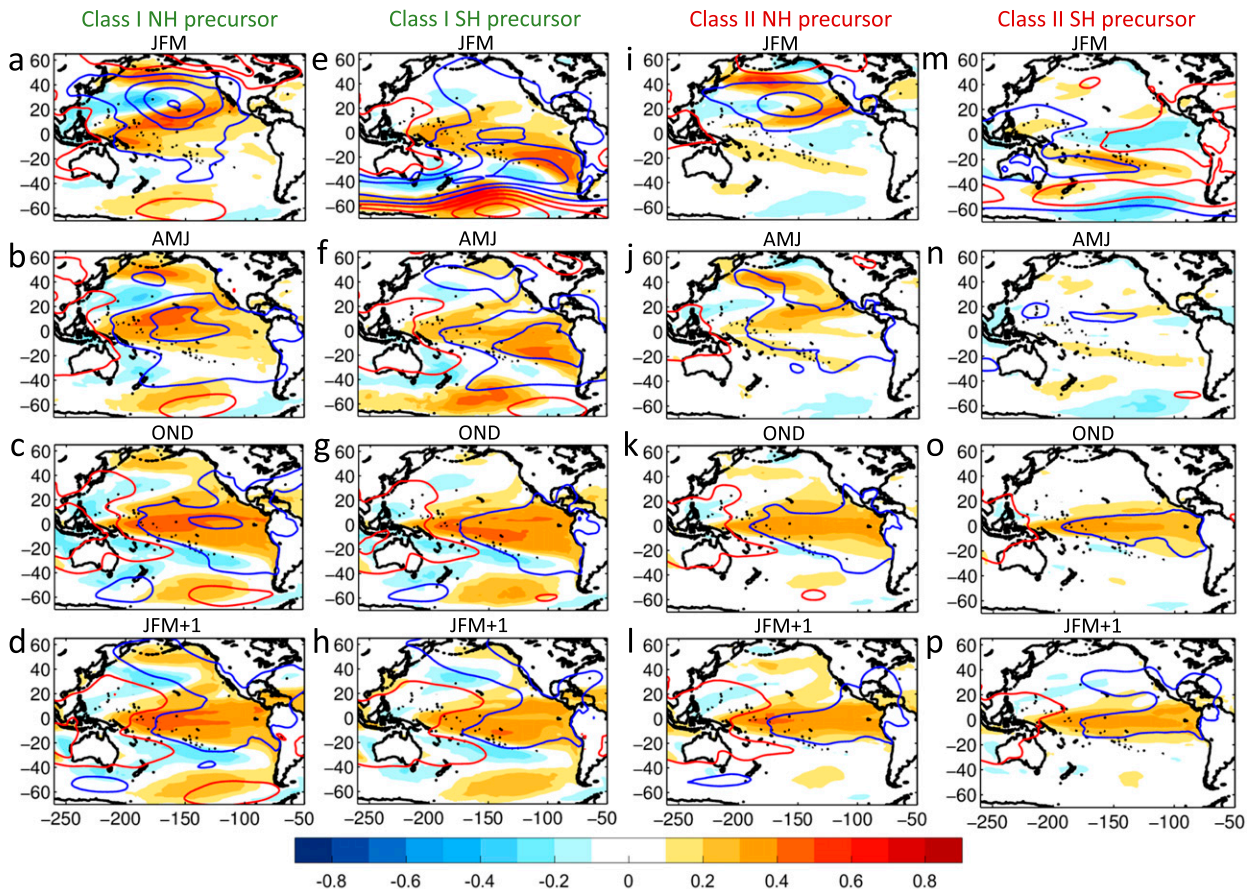


FIG. 13. Class I MEM seasonal progressions of the (first column) ENSO North Pacific precursor and (second column) ENSO South Pacific precursor. In the first column, the shadings show correlation maps between the NH SSTA precursor index and seasonal SSTA from (a) JFM to (d) the following JFM; the contours show the corresponding correlation maps between the NH SLPa precursor index and seasonal SLPa. The red contours show positive values, and the blue contours show negative values. Contours start from  $\pm 0.1$  and the interval is 0.2. The second column is like the first but shows correlation maps between the SH SSTA (SLPa) precursor index and seasonal SSTA (SLPa). (third column), (fourth column) As in the first two columns, but for Class II MEM seasonal progressions of northern and southern ENSO precursors, respectively.

SSST<sub>pre</sub>; blue bars in Fig. 14), northern and southern teleconnection indices (NSLP<sub>tele</sub> and SSLP<sub>tele</sub>, NSST<sub>tele</sub> and SSST<sub>tele</sub>; yellow bars in Fig. 14), and ENSO<sub>re</sub> index and ENSO index (green bars in Fig. 14) in both SSTA (Fig. 14a) and SLPa (Fig. 14b) fields to investigate the connections between dynamics of northern/southern extratropics and the tropics. The definitions of these indices are introduced in section 2. In the observations, the northern and southern precursor dynamics are independent of each other in both ocean and atmosphere ( $R < 0.1$ ; blue bars in Fig. 14, bottom row). However, the NP and SP successor patterns are strongly correlated because of the ENSO teleconnection ( $R > 0.6$ ; yellow bars in Fig. 14, bottom row). We test the extent to which the NP and SP precursors in the CMIP5 models are independent (e.g., a short blue bar indicates independence), their skill in reconstructing ENSO (green bars), and the coherence of the interhemispheric ENSO teleconnection patterns (yellow bars). Overall, northern–southern precursor correlations of the models range

from 0.09 (0) to 0.57 (0.51) for the SSTA (SLPa) pattern and are higher than that of the observation in 100% (80%) models (blue bars in Fig. 14). It suggests that precursor dynamics of NP and SP in some models are related to each other, likely through dynamics in the tropics. In 19 (20) out of 20 models, oceanic (atmospheric) teleconnections in the North Pacific and South Pacific are less related to each other compared to the observation (yellow bars in Fig. 14), which means ENSO teleconnections are weak in most models. The teleconnection responses are relatively more coherent across the hemispheres in most Class I models, with MEM correlations larger than Class II MEM in both SSTA field and SLPa field (Fig. 14), suggesting that ENSO teleconnections are relatively stronger in Class I models. The Class I MEM also shows higher correlations between northern and southern precursor indices and between ENSO<sub>re</sub> index and ENSO index than the Class II MEM (Fig. 14). To some extent, ENSO reconstructions can capture the variation of the ENSO index in most models, and

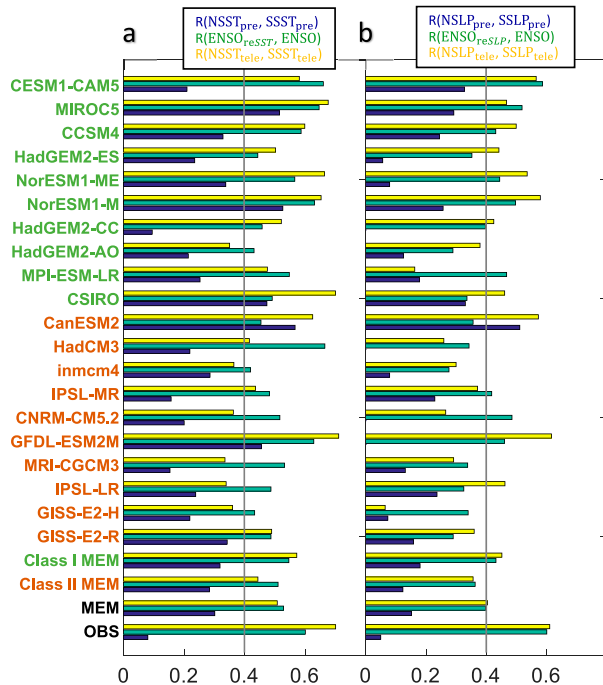


FIG. 14. (a) Correlation coefficients between  $NSST_{pre}$  and  $SSST_{pre}$  indices (blue bars),  $ENSO_{reSST}$  and ENSO indices (green bars), and  $NSST_{tele}$  and  $SSST_{tele}$  indices (yellow bars) of the OBS and individual simulations in CMIP5. (b) Correlation coefficients between  $NSLP_{pre}$  and  $SSLP_{pre}$  indices (blue bars),  $ENSO_{reSLP}$  and ENSO indices (green bars), and  $NSLP_{tele}$  and  $SSLP_{tele}$  indices (yellow bars) of the OBS and individual simulations in CMIP5. Models in Class I (II) are highlighted with green (red) fonts in the y axis.

correlations between these two indices of 20 (10) models are higher than 0.4 in the SST (SLP) field. Thus, extratropical precursor dynamics are connected with tropical ENSO variabilities, but the significance of the influence differs in models.

The interactions between the decadal variabilities of different regions (TPDV, PDV, and PREC) can be estimated by calculating the correlations between the corresponding indices (Fig. 15a). In the observations, TPDV can explain ~70% of the PDV ( $R = 0.83$ ; yellow bar of the bottom row in Fig. 15a). In 12 out of 20 CMIP5 models (including 8 Class I models and 4 Class II models), TPDV can explain more than 65% of the PDV (Fig. 15a, yellow bars), which is comparable with the observation. The observed PREC is highly correlated with PDV and TPDV ( $R > 0.8$ ; Fig. 15a, blue bar and green bar of the bottom row). However, the decadal extratropical precursor dynamics overall play less dominant roles in CMIP5 models, with correlations between PREC and TPDV exceeding 0.7 in only four models (CSIRO-Mk3.6.0, MPI-ESM-LR, HadCM3, IPSL-CM5A-LR) (Fig. 15a, green bars). Class I MEM shows higher correlation between PREC and TPDV than the Class II MEM (Fig. 15a), indicating that PREC plays more important role in the TPDV in Class I models. PREC is more connected to PDV than TPDV in nine models, which indicate that in these models, a significant portion of the PREC variability contributes

to the local decadal variance directly in the respective hemisphere. To study the connections between the reddening of the northern (southern) ENSO precursor dynamics and the PDV/TPDV, we applied an AR-1 model forced with  $NSST_{pre}$  ( $SSST_{pre}$ ) to obtain the low-frequency northern (southern) PREC indices [NPREC (SPREC)] and calculate the correlations between them and PDV/TPDV indices. The equations of NPREC/SPREC indices are:  $dNPREC(t)/dt = NSST_{pre}(t) - NPREC(t)/\tau$ ,  $dSPREC(t)/dt = SSST_{pre}(t) - SPREC(t)/\tau$ , where  $\tau = 1.2$  years. In observations, the NPREC play a more important role in TPDV/PDV than the SPREC (Figs. 15b,c, bottom rows). However, in the models, NP and SP precursors play an equally important role (Figs. 15b,c). This may be ascribed to the fact that these precursors are not as independent as in the observations.

## 6. Summary and discussion

In the observations, the interaction between tropical and extratropical dynamics integrates the extratropical seasonally varying stochastic forcing of the ENSO precursors into Pacific decadal-scale variance (Di Lorenzo et al. 2015; Zhao and Di Lorenzo 2020). The combinations of extratropical precursor indices show strong connections with ENSO ( $R = 0.6$ ) and the extratropical decadal variances can explain a large portion of TPDV and PDV (>64%) (Zhao and Di Lorenzo 2020). Based on the observational data from NCEP/NOAA and historical simulations of 20 CMIP5 models, we examine the TPDV and its decadal generation mechanisms linked to the sequence: ENSO precursors (extratropics) → ENSO (tropics) → ENSO successors (extratropics).

The selected CMIP5 models can reproduce the ENSO and ENSO teleconnections patterns (referred to as “successors”) (SCCs > 0.6), but the simulations of ENSO precursors are defective and inconsistent across models (Fig. 7). Nevertheless, the reconstructed ENSO indices using NP and SP precursors still show correlation with ENSO larger than 0.4 in most models (Fig. 14). About 80% of the models can capture the basic pattern of TPDV (SCCs > 0.6), but underestimate the spatial variance (Fig. 1). In most models, both interannual and decadal variances in the extratropics are weaker than those in the observations, and Class I models with better TPDV representation tend to display comparatively stronger extratropical variances (Figs. 3 and 8). Deser et al. (2012) also found that the linkage between the tropical and extratropical Pacific for both ENSO and PDV is weaker in CCSM4 than the observation. In CMIP5 models, the interannual connections between tropics and extratropics are important for better representing the decadal variability in the Pacific (Figs. 11 and 12). ENSO diversity is not discussed in this work, but the ENSO teleconnections can be strongly impacted by the tropical SSTa pattern (Capotondi et al. 2015). Both eastern Pacific ENSO (EP-ENSO) and central Pacific ENSO (CP-ENSO) have been shown to influence the extratropical variability of climate modes, the PDO (e.g., Yu and Kim 2011) and the NPGO (Di Lorenzo et al. 2010) respectively. However, in the low-frequency limit the distinction between PDO, NPGO, and TPDV is not very marked as they track different expression of

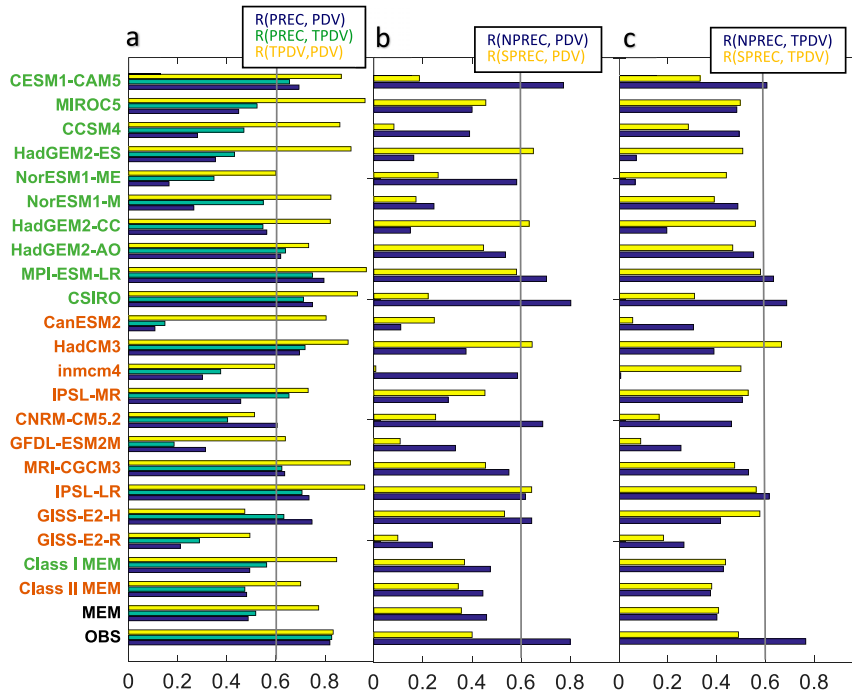


FIG. 15. (a) Correlation coefficients between PDV and PREC indices (blue bars), TPDV and PREC indices (green bars), and TPDV and PDV indices (yellow bars). (b) Correlation coefficients between PDV and NPREC indices (blue bars) and PDV and SPREC indices (yellow bars). (c) Correlation coefficients between TPDV and NPREC indices (blue bars) and TPDV and SPREC indices (yellow bars). Models in Class I (II) are highlighted with green (red) fonts on the y axis.

the low-frequency basic-scale Pacific dynamics (e.g., Di Lorenzo et al. 2015). As we discussed in the introduction, precursor dynamics can be initiated by stochastic forcing in both the extratropics and tropics. In this paper, we consider only the extratropical precursor dynamics because it is difficult to separate the precursor pattern and ENSO pattern in the tropics. Comparing Figs. 3d, 3i, and 3n, it is likely that tropical (extratropical) precursor dynamics in models play a more (less) important role in TPDV than in the observations.

Phase locking of ENSO is very important for the TPDV because the decadal hypothesis relies on the seasonality of ENSO: ENSO precursors (JFM)  $\rightarrow$  ENSO (NDJ)  $\rightarrow$  ENSO teleconnections (the following JFM). Among the CMIP5 models, some can capture the seasonal locking of ENSO (e.g., CCSM4, CESM1-CAM5); some show ENSO reaching its maximum in boreal spring (e.g., GFDL-ESM2M, MRI-CGCM3) or autumn (e.g., NorESM1-M/ME); and some reproduce the basic seasonal cycle but exhibit an abnormal peak in spring (e.g., HadGEM2-AO/CC/ES) or summer (e.g., INM-CM4), while some show significantly weak seasonal variation of ENSO (e.g., IPSL-CM5A-LR/MR) (Figs. 4e,f). Although ENSO seasonality is different among CMIP5 models, we define ENSO index as the first PC of NDJ SSTa in the tropical Pacific and define ENSO precursor patterns in the preceding JFM season in this paper. We also tried to define ENSO index in its maximum season in each model and find ENSO precursor

pattern in the preceding 9–10 months, but it did not lead to distinct different results.

We find that there are certain connections between skills in the representation of TPDV and ENSO precursor dynamics. Models that simulate better TPDV patterns usually are associated with better representations of the atmospheric precursor patterns (Figs. 10a,c). For oceanic precursors, in general, models have a better capability to reproduce the northern precursor (Fig. 9). Thus the representation of the southern precursor dynamics seems to be crucial for the intermodel differences in TPDV representation (Figs. 10b,d). The Class I MEM precursor pattern is similar to the observation, but models emphasize different aspects of the precursor dynamics (Fig. 11). In the observations, the NP oceanic precursor plays a more important role in Pacific decadal variance than the SP precursor (Figs. 15b,c, bottom row); one reason is the phase-locking between variances of atmosphere and ocean in the North Pacific. In the Southern Hemisphere, the wind variances are maximum in austral winter (JJA) whereas the SST variances maximize during austral summer (NDJ), which makes the oceanic response to the atmospheric stochastic forcing weaker than that in the North Pacific. However, in most of the CMIP5 models, the SP precursor seems to play an equally important role as the NP precursor (Figs. 15b,c), which is likely due to the larger correlation between these two precursors. This may also link to the biases in the South Pacific convergence

TABLE 4. Mean spatial correlation coefficients between patterns calculated for 1861–2004 and 1950–2004, averaged among 20 CMIP5 models.

Pattern	Correlation	Pattern	Correlation
SSTa ENSO	0.95	TPDV	0.86
SLPa ENSO	0.95	PREC	0.61
SSTa ENSO Pre	0.81	PDV	0.71
SLPa ENSO Pre	0.80		
SSTa ENSO Tele	0.95		
SLPa ENSO Tele	0.94		

zone (SPCZ) representation/double intertropical convergence zone (ITCZ) in CMIP5 models.

The simulation of the Pacific interdecadal–decadal variability in climate models is a key step to explore the potential predictability for the climate. Newman (2007) used a multivariate empirical model—the Linear Inverse Model (LIM) (Penland and Sardeshmukh 1995)—to investigate the predictability of the Pacific SST. The tropical–North Pacific coupling can improve the longer-term predictability, which is due to two stationary eigenmodes obtained from LIM. However, the CMIP3 models cannot well simulated these stationary eigenmodes (Newman 2007). Furtado et al. (2011) found that in CMIP3 models, the temporal and spatial statistics of PDO and NPGO show distinct discrepancies from the observation. Most CMIP3 models cannot accurately capture ENSO teleconnection dynamics from tropics to northern extratropics (Furtado et al. 2011). Our analyses also show that there is a large diversity in the simulation of decadal variances among the CMIP5 models, with some models showing defective capabilities in reproducing the TPDV and PDV patterns, and the ENSO teleconnections to the extratropics are weaker in CMIP5 models. Nidheesh et al. (2017) examined the influence of ENSO on PDO in CMIP3 and CMIP5 models. They found that ENSO teleconnection to the North Pacific is important to the interhemispheric pattern of the PDO. Lyu et al. (2016) indicated that some CMIP5 models cannot capture the interdecadal variability patterns in the Pacific. These studies emphasize the importance of ENSO and ENSO teleconnections because of the essential role of ENSO in shaping the Pacific decadal variability (e.g., Furtado et al. 2011; Newman 2007; Nidheesh et al. 2017). Previous studies also explored the origin of tropical Pacific decadal variability by suppressing variabilities in different regions of Pacific in climate models (Liu et al. 2002; Liguori and Di Lorenzo 2019; Chung et al. 2019). They found that dynamics in the extratropical Pacific play an important role in driving the tropical Pacific decadal variability. Specifically, suppressing the North Pacific dynamics reduces the tropical interannual variability significantly, while the absence of southern extratropical variability leads to no substantial reduction in ENSO but has a significant impact on the TPDV (Liguori and Di Lorenzo 2019; Chung et al. 2019). In this study, we investigate the impact of interactions between tropics and extratropics on the tropical Pacific decadal variability in CMIP5 models, with a focus on extratropical ENSO precursors. We find that the ENSO

precursor dynamics, especially the atmospheric precursor, seem to be equally important for the representation of the TPDV and PDV patterns. Thus, we suggest using models displaying realistic ENSO precursors to perform decadal prediction experiments.

This work organizes the behaviors of PDV/TPDV and the ENSO-related integration mechanism in CMIP5 climate models systematically, which can help us understand different components of the Pacific decadal variability and build the basis for decadal predictability in the Pacific. This study considered multiple models, but the runs are confined to historical simulations from 1861 to 2004. We also use model data from 1950 to 2004 to calculate the spatial patterns analyzed in this study, like ENSO, ENSO precursor, ENSO successor, TPDV, PDV, and PREC. Table 4 shows the spatial correlation coefficients between patterns calculate from these two different time periods, which are in general high (larger than 0.6). To maximize the confidence level of the decadal analysis, we used the whole available period of the simulations. Longer control simulations or ensembles of historical runs are potentially effective to distinguish the dynamic signal from the internal noise and increase the statistical reliability. It is also critical to further explore how these mechanisms are impacted by anthropogenic forcing. Large CMIP ensembles can be powerful tools to provide insight into the roles of both anthropogenic forcing and internal climate variability. We also propose to use empirical dynamical models (e.g., LIM; Penland and Sardeshmukh 1995) that can capture the key mechanisms that control PDV to evaluate the strength of the sequence ENSO precursors → ENSO → ENSO successors and to isolate the type of precursor dynamics that are active and dominant in each model.

*Acknowledgments.* This work is funded by the U.S. Department of Energy under Grant 350660B. The authors declare no competing interests. The authors acknowledge the Working Group of World Climate Research Programme (WCRP) on CMIP5 Coupled Modeling, as well as the Program for Climate Model Diagnosis and Intercomparison (PCMDI) for collecting and archiving the CMIP5 model output. We thank the various climate-modeling groups for producing and making their simulations available for analysis. The China Scholarship Council funded Y.Z.'s visiting at Georgia Institute of Technology.

*Data availability statement.* The observation data are available online: <https://www.esrl.noaa.gov/psd/data/gridded/data.noaa.ersst.v3.html> and <https://www.esrl.noaa.gov/psd/data/gridded/data.ncep.reanalysis.derived.surface.html>. CMIP5 model data are available online: <https://esgf-node.llnl.gov/projects/cmip5/>.

## REFERENCES

- Alexander, M. A., 1992: Midlatitude atmosphere–ocean interaction during El Niño. Part I: The North Pacific Ocean. *J. Climate*, **5**, 944–958, [https://doi.org/10.1175/1520-0442\(1992\)005<0944:MAIDEN>2.0.CO;2](https://doi.org/10.1175/1520-0442(1992)005<0944:MAIDEN>2.0.CO;2).
- , I. Bladé, M. Newman, J. R. Lanzante, N. C. Lau, and J. D. Scott, 2002: The atmospheric bridge: The influence of ENSO teleconnections on air–sea interaction over the global oceans.

- J. Climate*, **15**, 2205–2231, [https://doi.org/10.1175/1520-0442\(2002\)015<2205:TABTIO>2.0.CO;2](https://doi.org/10.1175/1520-0442(2002)015<2205:TABTIO>2.0.CO;2).
- , D. J. Vimont, P. Chang, and J. D. Scott, 2010: The impact of extratropical atmospheric variability on ENSO: Testing the seasonal footprinting mechanism using coupled model experiments. *J. Climate*, **23**, 2885–2901, <https://doi.org/10.1175/2010JCLI3205.1>.
- Anderson, B. T., 2003: Tropical Pacific sea-surface temperatures and preceding sea level pressure anomalies in the subtropical North Pacific. *J. Geophys. Res.*, **108**, 4732, <https://doi.org/10.1029/2003JD003805>.
- , R. C. Perez, and A. Karspeck, 2013: Triggering of El Niño onset through trade wind-induced charging of the equatorial Pacific. *Geophys. Res. Lett.*, **40**, 1212–1216, <https://doi.org/10.1002/grl.50200>.
- Bellenger, H., E. Guilyardi, J. Leloup, M. Lengaigne, and J. Vialard, 2014: ENSO representation in climate models: From CMIP3 to CMIP5. *Climate Dyn.*, **42**, 1999–2018, <https://doi.org/10.1007/s00382-013-1783-z>.
- Bratcher, A. J., and B. S. Giese, 2002: Tropical Pacific decadal variability and global warming. *Geophys. Res. Lett.*, **29**, 1918, <https://doi.org/10.1029/2002GL015191>.
- Bretherton, C. S., M. Widmann, V. P. Dymnikov, J. M. Wallace, and I. Bladé, 1999: The effective number of spatial degrees of freedom of a time-varying field. *J. Climate*, **12**, 1990–2009, [https://doi.org/10.1175/1520-0442\(1999\)012<1990:TENOSD>2.0.CO;2](https://doi.org/10.1175/1520-0442(1999)012<1990:TENOSD>2.0.CO;2).
- Capotondi, A., and Coauthors, 2015: Understanding ENSO diversity. *Bull. Amer. Meteor. Soc.*, **96**, 921–938, <https://doi.org/10.1175/BAMS-D-13-00117.1>.
- , P. D. Sardeshmukh, E. Di Lorenzo, A. C. Subramanian, and A. J. Miller, 2019: Predictability of US West Coast Ocean temperatures is not solely due to ENSO. *Sci Rep.*, **9**, 10993, <https://doi.org/10.1038/s41598-019-47400-4>.
- Chen, X., and J. M. Wallace, 2015: ENSO-like variability: 1900–2013. *J. Climate*, **28**, 9623–9641, <https://doi.org/10.1175/JCLI-D-15-0322.1>.
- Chen, Z., B. Gan, L. Wu, and F. Jia, 2018: Pacific–North American teleconnection and North Pacific Oscillation: Historical simulation and future projection in CMIP5 models. *Climate Dyn.*, **50**, 4379–4403, <https://doi.org/10.1007/s00382-017-3881-9>.
- Chiang, J. C. H., and D. J. Vimont, 2004: Analogous Pacific and Atlantic meridional modes of tropical atmosphere–ocean variability. *J. Climate*, **17**, 4143–4158, <https://doi.org/10.1175/JCLI4953.1>.
- Choi, J., S. I. An, J. S. Kug, and S. W. Yeh, 2011: The role of mean state on changes in El Niño’s flavor. *Climate Dyn.*, **37**, 1205–1215, <https://doi.org/10.1007/s00382-010-0912-1>.
- , —, S. W. Yeh, and J. Y. Yu, 2013: ENSO-like and ENSO-induced tropical Pacific decadal variability in CGCMs. *J. Climate*, **26**, 1485–1501, <https://doi.org/10.1175/JCLI-D-12-00118.1>.
- Chung, C. T., S. B. Power, A. Sullivan, and F. Delage, 2019: The role of the South Pacific in modulating tropical Pacific variability. *Sci. Rep.*, **9**, 18311, <https://doi.org/10.1038/s41598-019-52805-2>.
- Deser, C., M. A. Alexander, S. P. Xie, and A. S. Phillips, 2010: Sea surface temperature variability: Patterns and mechanisms. *Annu. Rev. Mar. Sci.*, **2**, 115–143, <https://doi.org/10.1146/annurev-marine-120408-151453>.
- , and Coauthors, 2012: ENSO and Pacific decadal variability in the Community Climate System Model version 4. *J. Climate*, **25**, 2622–2651, <https://doi.org/10.1175/JCLI-D-11-00301.1>.
- Di Lorenzo, E., and N. Mantua, 2016: Multi-year persistence of the 2014/15 North Pacific marine heatwave. *Nat. Climate Change*, **6**, 1042–1047, <https://doi.org/10.1038/nclimate3082>.
- , and Coauthors, 2008: North Pacific Gyre Oscillation links ocean climate and ecosystem change. *Geophys. Res. Lett.*, **35**, L08607, <https://doi.org/10.1029/2007GL032838>.
- , K. M. Cobb, J. C. Furtado, N. Schneider, B. T. Anderson, A. Bracco, M. A. Alexander, and D. J. Vimont, 2010: Central Pacific El Niño and decadal climate change in the North Pacific ocean. *Nat. Geosci.*, **3**, 762–765, <https://doi.org/10.1038/ngeo984>.
- , and Coauthors, 2013: Synthesis of Pacific Ocean climate and ecosystem dynamics. *Oceanography*, **26**, 68–81, <https://doi.org/10.5670/oceanog.2013.76>.
- , G. Liguori, N. Schneider, J. C. Furtado, B. T. Anderson, and M. A. Alexander, 2015: ENSO and meridional modes: A null hypothesis for Pacific climate variability. *Geophys. Res. Lett.*, **42**, 9440–9448, <https://doi.org/10.1002/2015GL066281>.
- Ding, R., J. Li, and Y. Tseng, 2015: The impact of South Pacific extratropical forcing on ENSO and comparisons with the North Pacific. *Climate Dyn.*, **44**, 2017–2034, <https://doi.org/10.1007/s00382-014-2303-5>.
- , —, —, C. Sun, and F. Xie, 2017: Joint impact of North and South Pacific extratropical atmospheric variability on the onset of ENSO events. *J. Geophys. Res. Atmos.*, **122**, 279–298, <https://doi.org/10.1002/2016JD025502>.
- England, M. H., and Coauthors, 2014: Recent intensification of wind-driven circulation in the Pacific and the ongoing warming hiatus. *Nat. Climate Change*, **4**, 222–227, <https://doi.org/10.1038/nclimate2106>.
- Fedorov, A. V., 2002: The response of the coupled tropical ocean–atmosphere to westerly wind bursts. *Quart. J. Roy. Meteor. Soc.*, **128**, 1–23, <https://doi.org/10.1002/qj.200212857901>.
- Furtado, J. C., E. Di Lorenzo, N. Schneider, and N. A. Bond, 2011: North Pacific decadal variability and climate change in the IPCC AR4 models. *J. Climate*, **24**, 3049–3067, <https://doi.org/10.1175/2010JCLI3584.1>.
- Garreaud, R., and D. S. Battisti, 1999: Interannual (ENSO) and interdecadal (ENSO-like) variability in the Southern Hemisphere tropospheric circulation. *J. Climate*, **12**, 2113–2123, [https://doi.org/10.1175/1520-0442\(1999\)012<2113:IEAIEL>2.0.CO;2](https://doi.org/10.1175/1520-0442(1999)012<2113:IEAIEL>2.0.CO;2).
- Ham, Y.-G., and J.-S. Kug, 2014: ENSO phase-locking to the boreal winter in CMIP3 and CMIP5 models. *Climate Dyn.*, **43**, 305–318, <https://doi.org/10.1007/s00382-014-2064-1>.
- Hsu, H.-H., and Y.-L. Chen, 2011: Decadal to bi-decadal rainfall variation in the western Pacific: A footprint of South Pacific decadal variability? *Geophys. Res. Lett.*, **38**, L03703, <https://doi.org/10.1029/2010GL046278>.
- Kalnay, E., and Coauthors, 1996: The NCEP/NCAR 40-Year Reanalysis Project. *Bull. Amer. Meteor. Soc.*, **77**, 437–471, [https://doi.org/10.1175/1520-0477\(1996\)077<0437:TNYRP>2.0.CO;2](https://doi.org/10.1175/1520-0477(1996)077<0437:TNYRP>2.0.CO;2).
- Karspeck, A. R., R. Seager, and M. A. Cane, 2004: Predictability of tropical Pacific decadal variability in an intermediate model. *J. Climate*, **17**, 2842–2850, [https://doi.org/10.1175/1520-0442\(2004\)017<2842:POTPDV>2.0.CO;2](https://doi.org/10.1175/1520-0442(2004)017<2842:POTPDV>2.0.CO;2).
- Kim, S. T., and J.-Y. Yu, 2012: The two types of ENSO in CMIP5 models. *Geophys. Res. Lett.*, **39**, L11704, <https://doi.org/10.1029/2012GL052006>.
- Knutson, T. R., and S. Manabe, 1998: Model assessment of decadal variability and trends in the tropical Pacific Ocean. *J. Climate*, **11**, 2273–2296, [https://doi.org/10.1175/1520-0442\(1998\)011<2273:MAODVA>2.0.CO;2](https://doi.org/10.1175/1520-0442(1998)011<2273:MAODVA>2.0.CO;2).

- Kosaka, Y., and S.-P. Xie, 2013: Recent global-warming hiatus tied to equatorial Pacific surface cooling. *Nature*, **501**, 403–407, <https://doi.org/10.1038/nature12534>.
- Kucharski, F., and Coauthors, 2016: Atlantic forcing of Pacific decadal variability. *Climate Dyn.*, **46**, 2337–2351, <https://doi.org/10.1007/s00382-015-2705-z>.
- Kwon, M., S.-W. Yeh, Y.-G. Park, and Y.-K. Lee, 2012: Changes in the linear relationship of ENSO–PDO under the global warming. *Int. J. Climatol.*, **33**, 1121–1128, <https://doi.org/10.1002/joc.3497>.
- Landerer, F. W., P. J. Gleckler, and T. Lee, 2014: Evaluation of CMIP5 dynamic sea surface height multi-model simulations against satellite observations. *Climate Dyn.*, **43**, 1271–1283, <https://doi.org/10.1007/s00382-013-1939-x>.
- Lee, T., D. E. Waliser, J.-L. F. Li, F. W. Landerer, and M. M. Gierach, 2013: Evaluation of CMIP3 and CMIP5 wind stress climatology using satellite measurements and atmospheric reanalysis products. *J. Climate*, **26**, 5810–5826, <https://doi.org/10.1175/JCLI-D-12-00591.1>.
- Liguori, G., and E. Di Lorenzo, 2019: Separating the North and South Pacific meridional modes contributions to ENSO and tropical decadal variability. *Geophys. Res. Lett.*, **46**, 906–915, <https://doi.org/10.1029/2018GL080320>.
- Linsley, B. K., G. M. Wellington, and D. P. Schrag, 2000: Decadal sea surface temperature variability in the subtropical South Pacific from 1726 to 1997 AD. *Science*, **290**, 1145–1148, <https://doi.org/10.1126/science.290.5494.1145>.
- Liu, Z., 2012: Dynamics of interdecadal climate variability: A historical perspective. *J. Climate*, **25**, 1963–1995, <https://doi.org/10.1175/2011JCLI3980.1>.
- , and E. Di Lorenzo, 2018: Mechanisms and predictability of Pacific decadal variability. *Curr. Climate Change Rep.*, **4**, 128–144, <https://doi.org/10.1007/s40641-018-0090-5>.
- , L. Wu, R. Gallimore, and R. Jacob, 2002: Search for the origins of Pacific decadal climate variability. *Geophys. Res. Lett.*, **29**, 1404, <https://doi.org/10.1029/2001GL013735>.
- Lyu, K., X. Zhang, J. A. Church, and J. Hu, 2016: Evaluation of the interdecadal variability of sea surface temperature and sea level in the Pacific in CMIP3 and CMIP5 models. *Int. J. Climatol.*, **36**, 3723–3740, <https://doi.org/10.1002/joc.4587>.
- Mantua, N. J., S. R. Hare, Y. Zhang, J. M. Wallace, and R. C. Francis, 1997: A Pacific interdecadal climate oscillation with impacts on salmon production. *Bull. Amer. Meteor. Soc.*, **78**, 1069–1079, [https://doi.org/10.1175/1520-0477\(1997\)078<1069:APICOW>2.0.CO;2](https://doi.org/10.1175/1520-0477(1997)078<1069:APICOW>2.0.CO;2).
- Martinez, E., D. Antoine, F. D’Ortenzio, and B. Gentili, 2009: Climate-driven basin-scale decadal oscillations of oceanic phytoplankton. *Science*, **326**, 1253–1256, <https://doi.org/10.1126/science.1177012>.
- McPhaden, M. J., and X. Yu, 1999: Equatorial waves and the 1997–98 El Niño. *Geophys. Res. Lett.*, **26**, 2961–2964, <https://doi.org/10.1029/1999GL004901>.
- Meehl, G. A., A. X. Hu, J. M. Arblaster, J. Fasullo, and K. E. Trenberth, 2013: Externally forced and internally generated decadal climate variability associated with the interdecadal Pacific oscillation. *J. Climate*, **26**, 7298–7310, <https://doi.org/10.1175/JCLI-D-12-00548.1>.
- , and Coauthors, 2014: Decadal climate prediction: An update from the trenches. *Bull. Amer. Meteor. Soc.*, **95**, 243–267, <https://doi.org/10.1175/BAMS-D-12-00241.1>.
- Mo, K. C., 2000: Relationships between low-frequency variability in the Southern Hemisphere and sea surface temperature anomalies. *J. Climate*, **13**, 3599–3610, [https://doi.org/10.1175/1520-0442\(2000\)013<3599:RBLFVI>2.0.CO;2](https://doi.org/10.1175/1520-0442(2000)013<3599:RBLFVI>2.0.CO;2).
- Moore, A. M., and R. Kleeman, 1996: The dynamics of error growth and predictability in a coupled model of ENSO. *Quart. J. Roy. Meteor. Soc.*, **122**, 1405–1446, <https://doi.org/10.1002/qj.49712253409>.
- Newman, M., 2007: Interannual to decadal predictability of tropical and North Pacific sea surface temperatures. *J. Climate*, **20**, 2333–2356, <https://doi.org/10.1175/JCLI4165.1>.
- , G. P. Compo, and M. A. Alexander, 2003: ENSO-forced variability of the Pacific decadal oscillation. *J. Climate*, **16**, 3853–3857, [https://doi.org/10.1175/1520-0442\(2003\)016<3853:EVOTPD>2.0.CO;2](https://doi.org/10.1175/1520-0442(2003)016<3853:EVOTPD>2.0.CO;2).
- , and Coauthors, 2016: The Pacific decadal oscillation, revisited. *J. Climate*, **29**, 4399–4427, <https://doi.org/10.1175/JCLI-D-15-0508.1>.
- Nidheesh, A. G., M. Lengaigne, J. Vialard, T. Izumo, A. S. Unnikrishnan, and C. Cassou, 2017: Influence of ENSO on the Pacific decadal oscillation in CMIP models. *Climate Dyn.*, **49**, 3309–3326, <https://doi.org/10.1007/s00382-016-3514-8>.
- Okumura, Y., 2013: Origins of tropical Pacific decadal variability: Role of stochastic atmospheric forcing from the South Pacific. *J. Climate*, **26**, 9791–9796, <https://doi.org/10.1175/JCLI-D-13-00448.1>.
- Park, J. H., S. I. An, S. W. Yeh, and N. Schneider, 2013: Quantitative assessment of the climate components driving the Pacific decadal oscillation in climate models. *Theor. Appl. Climatol.*, **112**, 431–445, <https://doi.org/10.1007/s00704-012-0730-y>.
- Penland, C., and P. D. Sardeshmukh, 1995: The optimal growth of tropical sea surface temperature anomalies. *J. Climate*, **8**, 1999–2024, [https://doi.org/10.1175/1520-0442\(1995\)008<1999:TOGOTS>2.0.CO;2](https://doi.org/10.1175/1520-0442(1995)008<1999:TOGOTS>2.0.CO;2).
- Power, S., T. Casey, C. Folland, A. Colman, and V. Mehta, 1999: Inter-decadal modulation of the impact of ENSO on Australia. *Climate Dyn.*, **15**, 319–324, <https://doi.org/10.1007/s003820050284>.
- Rodríguez-Fonseca, B., I. Polo, J. García-Serrano, T. Losada, E. Mohino, C. Roberto Mechoso, and F. Kucharski, 2009: Are Atlantic Niños enhancing Pacific ENSO events in recent decades? *Geophys. Res. Lett.*, **36**, L20705, <https://doi.org/10.1029/2009GL040048>.
- Roemmich, D., and J. McGowan, 1995: Climatic warming and the decline of zooplankton in the California Current. *Science*, **267**, 1324–1326, <https://doi.org/10.1126/science.267.5202.1324>.
- Rogers, J. C., 1981: The North Pacific oscillation. *Int. J. Climatol.*, **1**, 39–57, <https://doi.org/10.1002/joc.3370010106>.
- Smith, T. M., and R. W. Reynolds, 2004: Improved extended reconstruction of SST (1854–1997). *J. Climate*, **17**, 2466–2477, [https://doi.org/10.1175/1520-0442\(2004\)017<2466:IEROS>2.0.CO;2](https://doi.org/10.1175/1520-0442(2004)017<2466:IEROS>2.0.CO;2).
- Taylor, K. E., 2001: Summarizing multiple aspects of model performance in a single diagram. *J. Geophys. Res.*, **106**, 7183–7192, <https://doi.org/10.1029/2000JD900719>.
- , R. J. Stouffer, and G. A. Meehl, 2012: An overview of CMIP5 and the experiment design. *Bull. Amer. Meteor. Soc.*, **93**, 485–498, <https://doi.org/10.1175/BAMS-D-11-00094.1>.
- Trenberth, K. E., and J. W. Hurrell, 1994: Decadal atmosphere–ocean variations in the Pacific. *Climate Dyn.*, **9**, 303–319, <https://doi.org/10.1007/BF00204745>.
- Vimont, D. J., 2005: The contribution of the interannual ENSO cycle to the spatial pattern of decadal ENSO-like variability. *J. Climate*, **18**, 2080–2092, <https://doi.org/10.1175/JCLI3365.1>.

- , D. S. Battisti, and A. C. Hirst, 2001: Footprinting: A seasonal connection between the tropics and mid-latitudes. *Geophys. Res. Lett.*, **28**, 3923–3926, <https://doi.org/10.1029/2001GL013435>.
- , J. M. Wallace, and D. S. Battisti, 2003: The seasonal footprinting mechanism in the Pacific: Implications for ENSO. *J. Climate*, **16**, 2668–2675, [https://doi.org/10.1175/1520-0442\(2003\)016<2668:TSEMIT>2.0.CO;2](https://doi.org/10.1175/1520-0442(2003)016<2668:TSEMIT>2.0.CO;2).
- Watanabe, M., H. Shiogama, H. Tatebe, M. Hayashi, M. Ishii, and M. Kimoto, 2014: Contribution of natural decadal variability to global warming acceleration and hiatus. *Nat. Climate Change*, **4**, 893–897, <https://doi.org/10.1038/nclimate2355>.
- Yeh, S. W., and B. P. Kirtman, 2005: Pacific decadal variability and decadal ENSO amplitude modulation. *Geophys. Res. Lett.*, **32**, L05703, <https://doi.org/10.1029/2004GL021731>.
- Yi, D. L., B. Gan, L. Wu, and A. J. Miller, 2018: The North Pacific Gyre Oscillation and mechanisms of its decadal variability in CMIP5 models. *J. Climate*, **31**, 2487–2509, <https://doi.org/10.1175/JCLI-D-17-0344.1>.
- Yim, B. Y., M. Kwon, H. S. Min, and J.-S. Kug, 2014: Pacific decadal oscillation and its relation to the extratropical atmospheric variation in CMIP5. *Climate Dyn.*, **44**, 1521–1540, <https://doi.org/10.1007/s00382-014-2349-4>.
- Yu, J.-Y., and S. T. Kim, 2011: Relationships between extratropical sea level pressure variations and the central Pacific and eastern Pacific types of ENSO. *J. Climate*, **24**, 708–720, <https://doi.org/10.1175/2010JCLI3688.1>.
- Zhang, Y., J. M. Wallace, and D. S. Battisti, 1997: ENSO-like interdecadal variability: 1900–93. *J. Climate*, **10**, 1004–1020, [https://doi.org/10.1175/1520-0442\(1997\)010<1004:ELIV>2.0.CO;2](https://doi.org/10.1175/1520-0442(1997)010<1004:ELIV>2.0.CO;2).
- Zhao, Y., and E. Di Lorenzo, 2020: The impacts of extra-tropical ENSO precursors on tropical Pacific decadal-scale variability. *Sci. Rep.*, **10**, 3031, <https://doi.org/10.1038/s41598-020-59253-3>.